

RESEARCH ARTICLE SUMMARY

CANCER

Modulation of the proteostasis network promotes tumor resistance to oncogenic KRAS inhibitors

Xiangdong Lv†, Xuan Lu†, Jin Cao†, Qin Luo, Yao Ding, Fanglue Peng, Apar Pataer, Dong Lu, Dong Han, Eric Malmberg, Doug W. Chan, Xiaoran Wang, Sara R. Savage, Sufeng Mao, Jingjing Yu, Fei Peng, Liang Yan, Huan Meng, Laure Maneix, Yumin Han, Yiwen Chen, Wantong Yao, Eric C. Chang, Andre Catic, Xia Lin, George Miles, Pengxiang Huang, Zheng Sun, Bryan Burt, Huamin Wang, Jin Wang, Qizhi Cathy Yao, Bing Zhang, Jack A. Roth, Bert W. O'Malley, Matthew J. Ellis, Mothaffar F. Rimawi, Haoqiang Ying*, Xi Chen*

INTRODUCTION: KRAS is one of the most frequently mutated genes in human cancer. Despite advances in the development of inhibitors that directly target mutant KRAS and the approval of KRASG12C inhibitors sotorasib and adagrasib for the treatment of KRASG12C-mutant non-small cell lung cancer (NSCLC) patients, multiple lines of clinical and pre-clinical evidence demonstrate that adaptive resistance to KRAS inhibitors (KRASi) is rapid and almost inevitable. The heterogeneous resistance mechanisms in patients and dose-limiting toxicity associated with targeting multiple KRASi resistance pathways—such as receptor tyrosine kinases (RTKs), extracellular signal-regulated kinase (ERK), and AKT—remain a major barrier to progress.

RATIONALE: Most cancers require a balanced protein homeostasis (proteostasis) network to maintain oncogenic growth. Therapeutic insults often disrupt proteostasis and induce proteotoxic stresses. Residual drug-tolerant cells must overcome imbalances in the proteostasis network to maintain survival. How a proteostasis

network is orchestrated by driver oncogenes and the proteostasis reprogramming mechanisms that bypass oncogene addiction and allow for acquired resistance to targeted therapies remain largely unknown. In this study, we investigated the regulation of proteostasis by oncogenic KRAS and the rewiring of proteostasis network underlying the acquired resistance to KRAS inhibition.

RESULTS: We show that oncogenic KRAS is critical for protein quality control in cancer cells. Genetic or pharmacological inhibition of oncogenic KRAS rapidly inactivated both cytosolic and endoplasmic reticulum (ER) protein quality control machinery, two essential components of the proteostasis network, through inhibition of the master regulators heat shock factor 1 (HSF1) and inositol-requiring enzyme 1α (IRE1α). However, residual cancer cells that survive KRASi directly reactivated IRE1α through an ER stress-independent phosphorylation mechanism that reestablished proteostasis and sustained acquired resistance to KRAS inhibition. We identified four onco-

genic signaling-regulated phosphorylation sites in IRE1α (Ser⁵²⁵, Ser⁵²⁹, Ser⁵⁴⁹, and Thr⁹⁷³) that are distinct from IRE1α autophosphorylation sites but are required for enhanced protein stability. The phosphorylation of IRE1α at these sites prevents IRE1α binding with the SEL1L/HRD1 E3 ligase complex, thus impairing the ubiquitination-dependent degradation of IRE1α and stabilizing the protein. These sites are the convergence points of multiple resistance mechanisms in KRASi-resistant tumors. RTK-mediated reactivation of ERK and hyperactivation of AKT sustained the unconventional phosphorylation of IRE1α in the KRASi-resistant tumors, which consequently restored its protein stability and reestablished proteostasis. Genetic or pharmacological suppression of IRE1α collapsed the rewired proteostasis network and overcame resistance to KRAS-MAPK (mitogen-activated protein kinase) inhibitors.

CONCLUSION: This study reveals the direct cross-talk between oncogenic signaling and the protein quality control machinery and uncovers the mechanisms that account for the proteostasis rewiring in response to KRAS inhibition. Multiple resistance mechanisms converge on IRE1α through ER stress-independent phosphorylation to restore proteostasis and promote KRASi-resistant tumor growth. Targeting this key convergence point represents an effective therapeutic strategy to overcome KRASi resistance. ■

The list of author affiliations appears in the full article online.

*Corresponding author. Email: xi.chen@bcm.edu (X.C.); hying@mdanderson.org (H.Y.)

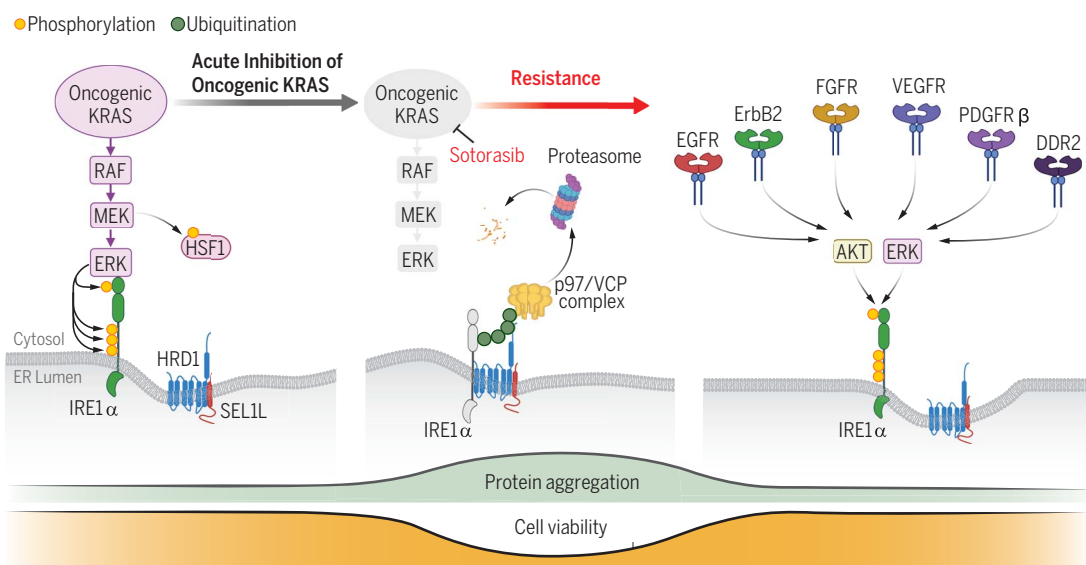
†These authors contributed equally to this work.

Cite this article as X. Lv et al., *Science* **381**, eabn4180 (2023). DOI: 10.1126/science.abn4180

S READ THE FULL ARTICLE AT
<https://doi.org/10.1126/science.abn4180>

Proteostasis reprogramming upon KRAS inhibition

Inhibition of oncogenic KRAS inactivates both cytosolic and ER protein quality control machinery by inhibiting HSF1 and IRE1α. Residual cells that survive KRASi directly restore IRE1α phosphorylation through receptor tyrosine kinase-mediated reactivation of ERK and hyperactivation of AKT, preventing IRE1α from SEL1L/HRD1-mediated ubiquitination and degradation. Multiple heterogeneous resistance pathways converge on IRE1α to reestablish proteostasis and promote resistance to KRASi.



RESEARCH ARTICLE

CANCER

Modulation of the proteostasis network promotes tumor resistance to oncogenic KRAS inhibitors

Xiangdong Lv^{1,2,3†}, Xuan Lu^{1,2,3†}, Jin Cao^{1,2,3†}, Qin Luo^{1,2,3}, Yao Ding^{1,2,3}, Fanglue Peng^{1,2,3}, Apar Pataer⁴, Dong Lu^{1,5,6}, Dong Han^{1,2,3}, Eric Malmberg^{1,2,3}, Doug W. Chan^{1,2,3}, Xiaoran Wang^{1,2,3}, Sara R. Savage^{2,3,7}, Sufeng Mao^{1,2,3}, Jingjing Yu^{1,2,3}, Fei Peng^{1,8}, Liang Yan⁹, Huan Meng¹, Laure Maneix^{1,10}, Yumin Han^{1,2,3}, Yiwen Chen¹¹, Wantong Yao¹², Eric C. Chang^{1,2,3}, Andre Catic^{1,10}, Xia Lin¹³, George Miles^{2,3,7}, Pengxiang Huang¹, Zheng Sun^{1,8}, Bryan Burt¹⁴, Huamin Wang¹⁵, Jin Wang^{1,5,6}, Qizhi Cathy Yao¹³, Bing Zhang^{2,3,7}, Jack A. Roth⁴, Bert W. O'Malley¹, Matthew J. Ellis^{2,3,16}, Mothaffar F. Rimawi^{2,3}, Haoqiang Ying^{8*}, Xi Chen^{1,2,3*}

Despite substantial advances in targeting mutant KRAS, tumor resistance to KRAS inhibitors (KRASi) remains a major barrier to progress. Here, we report proteostasis reprogramming as a key convergence point of multiple KRASi-resistance mechanisms. Inactivation of oncogenic KRAS down-regulated both the heat shock response and the inositol-requiring enzyme 1α (IRE1α) branch of the unfolded protein response, causing severe proteostasis disturbances. However, IRE1α was selectively reactivated in an ER stress-independent manner in acquired KRASi-resistant tumors, restoring proteostasis. Oncogenic KRAS promoted IRE1α protein stability through extracellular signal-regulated kinase (ERK)-dependent phosphorylation of IRE1α, leading to IRE1α disassociation from 3-hydroxy-3-methylglutaryl reductase degradation (HRD1) E3-ligase. In KRASi-resistant tumors, both reactivated ERK and hyperactivated AKT restored IRE1α phosphorylation and stability. Suppression of IRE1α overcame resistance to KRASi. This study reveals a druggable mechanism that leads to proteostasis reprogramming and facilitates KRASi resistance.

KRAS is one of the most frequently mutated genes in human cancer, especially in pancreatic ductal adenocarcinoma (PDAC), non-small cell lung cancer (NSCLC), and colorectal carcinoma (CRC) (1–5). Onco-

genic KRAS engages multiple effector pathways to drive tumorigenesis, notably the RAF/MEK/ERK (MAPK) and phosphatidylinositol 3-kinase (PI3K)/AKT pathways (6–10). Small molecules that directly target the KRAS G12C mutation (in which glycine at position 12 is replaced by cysteine), including sotorasib and adagrasib (11–13), have shown encouraging therapeutic efficacies in clinical trials (14–16). The US Food and Drug Administration (FDA) granted accelerated approval for sotorasib and adagrasib to treat patients with KRAS^{G12C}-mutant NSCLC. However, resistance to these KRAS inhibitors (KRASi) is almost inevitable, resulting from the activation of compensatory pathways—such as epidermal growth factor (EGF), fibroblast growth factor (FGF), aurora kinase A (AURKA), or SOS1—or the acquisition of new mutations, such as KRAS, NRAS, BRAF, EGFR, or FGFR2 (15–35). Although inhibitors that target KRAS mutations other than G12C are in clinical trials (36), similar bypass of KRAS dependence has been demonstrated in preclinical studies that used genetically engineered mouse models (GEMMs) of lung and pancreatic cancer (37–39). Because of these clinical challenges, understanding the mechanisms that mediate the resistance to KRASi is imperative to develop more effective therapies to prevent the recurrence of KRAS-driven cancers.

The ability to overcome an imbalanced protein homeostasis or “proteostasis” network is

instrumental to maintain cancer cell survival and circumvent various insults that impair the quality of protein synthesis and folding (40, 41). Cells use compartment-specific stress sensors to monitor and maintain a high-fidelity proteome. Cytosolic proteins are monitored by the heat shock response (HSR) (42), whereas transmembrane and secreted proteins are monitored in the endoplasmic reticulum (ER) by the unfolded protein response (UPR) (43–45). When the HSR is triggered by stress stimuli, heat shock factors (HSFs) become activated and transactivate genes that encode chaperones and other factors of the proteostasis network (46). HSF1 is a master regulator of the proteotoxic stress response and has been implicated in mediating proteome fidelity in cancer cells (47). The UPR is a three-branched stress response that is activated upon disruption of ER homeostasis. The UPR is mediated by the ER transmembrane sensors inositol-requiring enzyme 1α (IRE1α), activated transcription factor 6 (ATF6), and protein kinase RNA-like ER kinase (PERK) (48). IRE1α is the most ancient and conserved member of the mammalian UPR sensory triad (49, 50). Under ER stress conditions, IRE1α undergoes oligomerization and trans-autophosphorylation to activate its ribonuclease (RNase) domain. This results in excision of 26 nucleotides from unspliced *XBPI* (*XBPIu*) mRNA, and a frame shift mutation to produce the mature, spliced *XBPI* (*XBPIs*), which encodes a potent transcriptional activator (fig. S1A) (51, 52). Mutant RAS was traditionally viewed as an inducer of general UPR through stressing ER during oncogenic transformation of nonmalignant cells (53). Genetic screens revealed the synthetic lethal interaction between mutant RAS and IRE1α in yeast (54). Yet it remains unclear how the proteostasis network is orchestrated by oncogenic KRAS, or how the proteostasis reprogramming mechanisms occur that bypass KRAS addiction and allow for acquired resistance to KRASi.

Here, we report that proteostasis is dynamically altered upon oncogenic KRAS inhibition. We identified the IRE1α-mediated reprogramming of proteostasis as an essential mechanism that facilitates resistance to KRAS-MAPK inhibition. We also elucidated the biochemical basis for the ER stress-independent post-translational modification and regulation of IRE1α through both oncogenic KRAS signaling and KRASi resistance signaling, which serves as a therapeutic vulnerability that can be targeted to overcome resistance to KRAS-MAPK inhibition.

Oncogenic KRAS inactivation reprograms proteostasis

To understand the impacts of oncogenic KRAS on proteostasis, we used primary mouse PDAC cells derived from our previously generated,

¹Department of Molecular and Cellular Biology, Baylor College of Medicine, Houston, TX 77030, USA. ²Lester and Sue Smith Breast Center, Baylor College of Medicine, Houston, TX 77030, USA. ³Dan L. Duncan Comprehensive Cancer Center, Baylor College of Medicine, Houston, TX 77030, USA. ⁴Department of Thoracic and Cardiovascular Surgery, University of Texas MD Anderson Cancer Center, Houston, TX 77030, USA. ⁵Department of Pharmacology and Chemical Biology, Baylor College of Medicine, Houston, TX 77030, USA. ⁶Center for Drug Discovery, Baylor College of Medicine, Houston, TX 77030, USA. ⁷Department of Molecular and Human Genetics, Baylor College of Medicine, Houston, TX 77030, USA. ⁸Department of Medicine, Division of Diabetes, Endocrinology and Metabolism, Baylor College of Medicine, Houston, TX 77030, USA. ⁹Department of Molecular and Cellular Oncology, University of Texas MD Anderson Cancer Center, Houston, TX 77030, USA. ¹⁰Huntington Center on Aging, Baylor College of Medicine, USA. ¹¹Department of Bioinformatics and Computational Biology, University of Texas MD Anderson Cancer Center, Houston, TX 77030, USA. ¹²Department of Translational Molecular Pathology, University of Texas MD Anderson Cancer Center, Houston, TX 77030, USA. ¹³Division of Surgical Oncology, Michael E. DeBakey Department of Surgery, Baylor College of Medicine, Houston, TX 77030, USA. ¹⁴Division of Thoracic Surgery, Michael E. DeBakey Department of Surgery, Baylor College of Medicine, Houston, TX 77030, USA. ¹⁵Department of Pathology, University of Texas MD Anderson Cancer Center, Houston, TX 77030, USA. ¹⁶Early Oncology, Oncology R&D, AstraZeneca, Gaithersburg, MD, USA.
*Corresponding author. Email: xi.chen@bcm.edu (X.C.); hying@mdanderson.org (H.Y.)
†These authors contributed equally to this work.

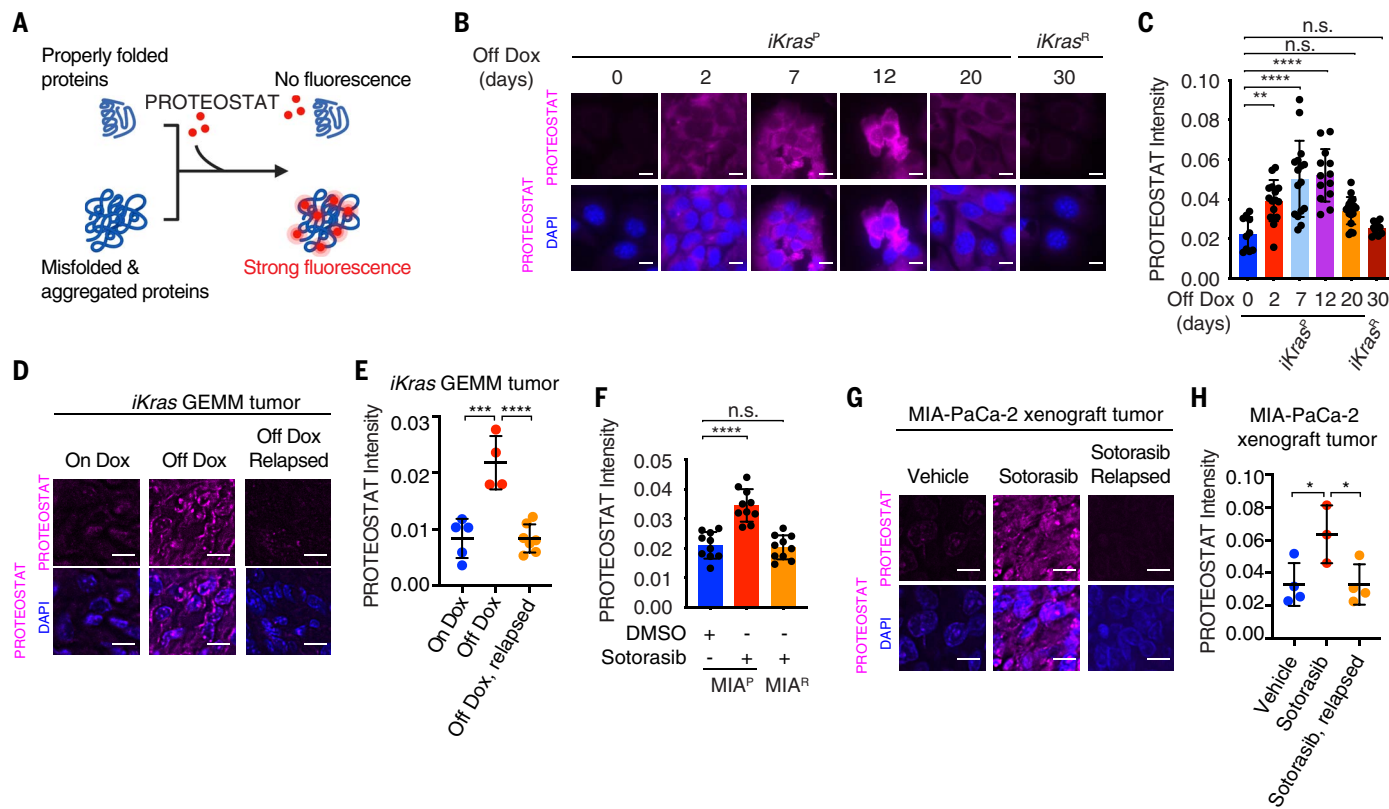


Fig. 1. Oncogenic KRAS inactivation reprograms proteostasis. (A) Schematic illustration of labeling and detection of misfolded and aggregated proteins with PROTEOSTAT dye. Upon intercalation into the cross- β spine typically found in misfolded and aggregated proteins, PROTEOSTAT dye emits strong fluorescence. (B) Representative images and (C) quantification of PROTEOSTAT (magenta) and 4',6-diamidino-2-phenylindole (DAPI) (blue) staining in *iKras^P* cells at different time points after *Kras^{G12D}* inactivation through Dox-withdrawal (Off Dox) until the cells acquired resistance to *Kras^{G12D}* inactivation (*iKras^R* cell). (D) Representative images and (E) quantification of PROTEOSTAT (magenta) staining in spontaneous tumors from the Dox-inducible, *Kras^{G12D}*-driven PDAC mouse model (*iKras* GEMM) treated with doxycycline (Dox, 2 g/liter, $n = 5$ mice), Dox withdrawal for 3 days ($n = 4$ mice) or relapsed after 30 weeks of Dox-withdrawal ($n = 7$ mice). (F) Quantification of PROTEOSTAT intensity in parental

MIA-PaCa-2 (*MIA^P*) cells treated with dimethyl sulfoxide (DMSO) or 30 nM sotorasib for 2 days or in sotorasib-resistant *MIA-PaCa-2* (*MIA^R*) cells treated with 30 nM sotorasib. *MIA^R* cells were generated in vitro by means of continued sotorasib treatment until the cells acquired resistance. (G) Representative images and (H) quantification of PROTEOSTAT (magenta) and DAPI (blue) staining in *MIA-PaCa-2* xenograft tumors treated with vehicle ($n = 4$ mice), sotorasib (30 mg/kg for 1 day, $n = 3$ mice), or relapsed after 9 weeks of sotorasib treatment (30 mg/kg, $n = 4$ mice). Data represent average fluorescence intensity of PROTEOSTAT per cell from each image [(C) and (F)] or tumor [(E) and (H)] and are presented as mean \pm SD from $n \geq 10$ images. Scale bar, 20 μ m. Ordinary one-way analysis of variance (ANOVA) with Dunnett's multiple comparisons test in (C), (E), (F), and (H) was used to calculate P values. n.s., not significant, * $P < 0.05$, ** $P < 0.01$, *** $P < 0.001$, **** $P < 0.0001$.

doxycycline (Dox)-inducible, *Kras^{G12D}*-driven PDAC mouse model (55), which are hereafter designated as *iKras* cells. Dox withdrawal turned off *Kras^{G12D}* expression in *iKras* cells (fig. S1B), resulting in the inactivation of downstream MAPK signaling (fig. S1C), decreased 5-bromodeoxyuridine (BrdU) incorporation (fig. S1D), and increased cell apoptosis (fig. S1E). We monitored protein aggregation upon *Kras^{G12D}* inactivation using PROTEOSTAT, a molecular rotor dye that specifically intercalates into the cross- β spines of the quaternary protein structures found in misfolded and aggregated proteins (Fig. 1A). As a positive control, the treatment of *iKras* cells with the proteasome inhibitor MG132 significantly induced PROTEOSTAT signal (fig. S1F). The inactivation of *Kras^{G12D}* from Dox withdrawal induced protein aggregation (Fig. 1, B and C). However, 30 days after Dox withdrawal, *iKras*

cells displayed restored proteostasis (Fig. 1, B and C) and resumed cell growth (fig. S1, D, E, and G), at levels comparable with those observed for parental cells (*iKras^P*). These cells resistant to *Kras^{G12D}* inactivation are hereafter designated as *iKras^R* cells. Continuous *Kras^{G12D}* inactivation was required to maintain the resistance phenotypes because reactivation of *Kras^{G12D}* for extended periods (12 days) partially reversed the resistance of *iKras^R* cells to Dox withdrawal (fig. S1, H to K). Dox administration had no impact on cell growth or proteostasis in *LSL-Kras^{G12D}* cells that lack Dox-inducible *Kras^{G12D}* expression (fig. S1, L to P). In the *iKras* cells, staining with Congo red (CR) or thioflavin T (ThT), which recognize misfolded protein aggregates (56), or detection of lysine 48 (K48)-linked polyubiquitin levels, which tag misfolded or aggregated proteins for proteasome-mediated degradation (57), independently con-

firmed the restoration of proteostasis upon acquired resistance to *Kras^{G12D}* inactivation (fig. S1, Q to S).

We also used the *iKras* GEMM to examine *in vivo* proteostasis reprogramming (55). *Kras^{G12D}* inactivation through Dox withdrawal resulted in rapid tumor regression, but 70% of tumors relapsed after 9 to 47 weeks (37). PROTEOSTAT staining of *iKras* GEMM tumors at different stages of *Kras^{G12D}* inactivation revealed increased protein aggregation in regressing parental tumors and restored proteostasis in relapsed tumors (Fig. 1, D and E, and fig. S2A), which grow independently of *Kras^{G12D}* expression.

To further investigate the impacts of oncogenic KRAS inhibition on proteostasis, we used a KRAS^{G12C} inhibitor, sotorasib (12), to treat *MIA-PaCa-2* human PDAC cells and H358 human NSCLC cells harboring the *KRAS^{G12C}*

mutation. Sotorasib effectively suppressed the activation of MEK/ERK (fig. S2, B and C), leading to cell growth inhibition in both MIA-PaCa-2 and H358 cell lines (fig. S2, D and E). Both MIA-PaCa-2 and H358 cells also displayed increased PROTEOSTAT staining and K48-linked polyubiquitination levels in response to sotorasib treatment, suggesting enhanced protein aggregation (Fig. 1F and fig. S2, F to H). However, after MIA-PaCa-2 and H358 cells gained resistance to sotorasib (fig. S2, D and E), they also exhibited restored proteostasis (Fig. 1F and fig. S2, F to H). Similar to *iKras^R* cells, continuous sotorasib treatment was required to maintain the resistance of MIA-PaCa-2^R cells to KRASi (fig. S2, I and J). MIA-PaCa-2 xenograft tumors were initially sensitive to sotorasib treatment but relapsed after 6 weeks (fig. S2K). PROTEOSTAT staining revealed increased protein aggregation after initial sotorasib treatment and restored proteostasis in relapsed tumors (Fig. 1, G and H). These data demonstrate that oncogenic KRAS inhibition induces protein aggregation and severely disrupts proteostasis. However, KRASi-resistant cancer cells able to grow in the absence of mutant KRAS gain the capacity to overcome associated proteotoxic stress and regain proteostasis.

Oncogenic KRAS inactivation differentially affects the key nodes of proteostasis regulatory network

Proteostasis is maintained by an integrated network that includes translation, protein quality control mechanisms that regulate the content and quality of the proteome, and protein degradation pathways, such as the ubiquitin-proteasome system and the autophagy-lysosome system, which eliminate misfolded or aggregated proteins (42, 43, 58). *Kras^{G12D}* inactivation through Dox withdrawal in *iKras* cells did not alter overall proteasomal activity (fig. S3, A and B). We observed increased LC3 cleavage and lysosome-associated membrane protein type 1 (LAMP1) levels upon *Kras^{G12D}* inactivation (fig. S3C), indicating elevated autophagy and lysosomal activities, which unlikely caused increased protein aggregation. Next, we examined the protein quality control and stress response pathways that monitor and regulate protein folding, including the UPR and HSR. *Kras^{G12D}* inactivation in *iKras^P* cells markedly reduced IRE1 α protein levels, *Xbp1* splicing, and the expression levels of the XBP1s targets *Edem1* and *Sec61a1* (Fig. 2A and fig. S3, D to F). As a control, Dox treatment had no impacts on IRE1 α levels in the constitutively activated *Lsl-Kras^{G12D}* cells (fig. S3G). By contrast, ATF6 was barely affected, and phospho-PERK was negatively correlated with IRE1 α /XBP1 in response to *Kras^{G12D}* inactivation (Fig. 2A). Resolving protein aggregation with tauroursodeoxycholic acid (TUDCA), a chemical chaperone that promotes protein folding and stimulates

molecular chaperone function (59, 60), completely blunted *Kras^{G12D}* inactivation-induced phospho-PERK (fig. S3, H to J), indicating that PERK was activated as a result of the disrupted proteostasis by KRASi. PERK is one of the four kinases [general control nonderepressible 2 (GCN2), PERK, heme-regulated inhibitor (HRI), and RNA-activated protein kinase (PKR)] that phosphorylate eIF2 α and regulate the integrated stress response (ISR) (61). Unexpectedly, eIF2 α and its downstream ATF4 followed an opposite pattern as that of phospho-PERK upon *Kras^{G12D}* inactivation (Fig. 2A). *Perk* deletion had no effects on their levels (fig. S3K). Genetic deletion of each ISR kinases demonstrated that phospho-eIF2 α and ATF4 were dependent on GCN2, which was activated in *iKras^P* cells (Fig. 2A and fig. S3K). These data establish GCN2 as a regulator of ISR in this context. IRE1 α /XBP1, but not GCN2 or eIF2 α , was selectively restored in *iKras^R* cells (Fig. 2A and fig. S3, D to F). Consistently, sotorasib treatment reduced IRE1 α protein levels in MIA-PaCa-2 and H358 cells, but IRE1 α was restored after the acquisition of sotorasib resistance (Fig. 2, B and C, and fig. S2, D and E). IRE1 α immunostaining in the parental, *Kras^{G12D}*-extincted, relapsed *iKras* GEMM tumors (Fig. 2D) and sotorasib-treated MIA-PaCa-2 human xenograft tumors (Fig. 2E) all independently confirmed the in vivo pattern of acute IRE1 α suppression followed by reactivation in relapsed tumors. We also confirmed the continuous in vivo suppression of phospho-GCN2, phospho-eIF2 α , and ATF4 through sotorasib treatment in MIA-PaCa-2 xenograft tumors (fig. S3L). Collectively, these data show that acute oncogenic KRAS inactivation inhibits the IRE1 α branch of the UPR and GCN2-regulated ISR. However, only IRE1 α is reactivated in the KRASi-resistant tumors.

In contrast with our findings on IRE1 α , sotorasib continuously suppressed HSF1 phosphorylation at serine residue 326 (S326), which is required for HSF1 activation (62), in both parental and sotorasib-resistant MIA-PaCa-2 and H358 cells (Fig. 2, B and C). The inhibitory phosphorylation of HSF1 at S121 (62) was increased in both sotorasib-resistant MIA-PaCa-2^R and H358^R cells (Fig. 2, B and C). As a result, sotorasib treatment markedly reduced the expression of HSF1 target genes, including *Hspa6* and *Hspa1b*, in both parental and sotorasib-resistant MIA-PaCa-2 and H358 cells (fig. S3, M and N). We confirmed the in vivo suppression of HSF1-S326 phosphorylation by means of sotorasib treatment in MIA-PaCa-2 human xenograft tumors (Fig. 2E) and marked reduction of HSF1 luciferase reporter activities in sotorasib-resistant MIA-PaCa-2^R cells (fig. S3, O and P). The genetic inactivation of *Kras^{G12D}* also resulted in the considerable reduction of HSF1 luciferase reporter activities in both *iKras^P* and *iKras^R* cells (Fig. 2F). Collectively, these data

demonstrate that oncogenic KRAS inactivation initially impairs both the ER and cytosolic protein quality control machinery as well as the ISR. However, only IRE1 α /XBP1, but not HSF1 or ISR, is restored in the KRASi-resistant tumors.

IRE1 α /XBP1 is required for maintaining proteostasis in KRASi-resistant cancer cells

Next, we examined the necessity of IRE1 α /XBP1 for proteostasis maintenance. In *iKras^P* cells, *Irela* and *Xbp1* depletion modestly induced protein aggregation (Fig. 2, G and H, and fig. S4A), with minimal effects on cell growth (Fig. 2I). By contrast, *Irela* and *Xbp1* depletion in the *iKras^R* cells led to profound protein aggregation and PERK phosphorylation (Fig. 2, G and H, and fig. S4, A to F) and significantly inhibited cell growth (Fig. 2I). These effects were rescued by TUDCA (Fig. 2, G to I, and fig. S4B), demonstrating the importance of IRE1 α /XBP1 in the maintenance of proteostasis and cell survival. Depletion of *Perk* did not affect proteostasis and cell growth of *iKras^R* cells and had no impacts on *Irela* depletion-induced phenotypes (fig. S4, G to K), suggesting that PERK is dispensable for KRASi-resistant cancer cells. The kinase activity of IRE1 α is required for its RNase activation (63). In contrast to wild-type (WT) IRE1 α , neither kinase-dead IRE1 α^{K599A} nor RNase-dead IRE1 α^{K907A} mutant (63) was able to rescue *Irela* depletion-induced phenotypes in *iKras^R* cells (fig. S5, A to D), suggesting that IRE1 α 's function depends on its catalytic RNase activity. In addition to XBP1s, IRE1 α RNase also cleaves ER-localized RNAs through the regulated IRE1 α -dependent decay (RIDD) pathway (64, 65). Although some RIDD targets were regulated by IRE1 α (fig. S5, E and F), restoration of XBP1s completely rescued the *Irela* depletion-induced protein aggregation and cell growth defects in *iKras^R* cells (fig. S5, G to I). These data establish that IRE1 α RNase activity and RNase-dependent XBP1 splicing drives proteostasis in KRASi-resistant cancer cells. Consistently, CRISPR-mediated *Irela* or *Xbp1* deletion (fig. S5J) resulted in more severe protein aggregation in *iKras^R* cells than in *iKras^P* cells (fig. S5K). Taken together, we demonstrate that IRE1 α /XBP1 is indispensable for the maintenance of balanced proteostasis in KRASi-resistant cancer cells.

The MAPK pathway regulates IRE1 α /XBP1 in parental KRAS-driven cancer cells

We aimed to determine the mechanism through which oncogenic KRAS regulates IRE1 α . MAPK and PI3K are two major effector pathways downstream of oncogenic KRAS (6). The MEK inhibitor trametinib and the ERK inhibitor SCH772984 both substantially reduced IRE1 α protein levels in *iKras^P* cells (Fig. 3A). By contrast, the PI3K inhibitor pictilisib and the AKT

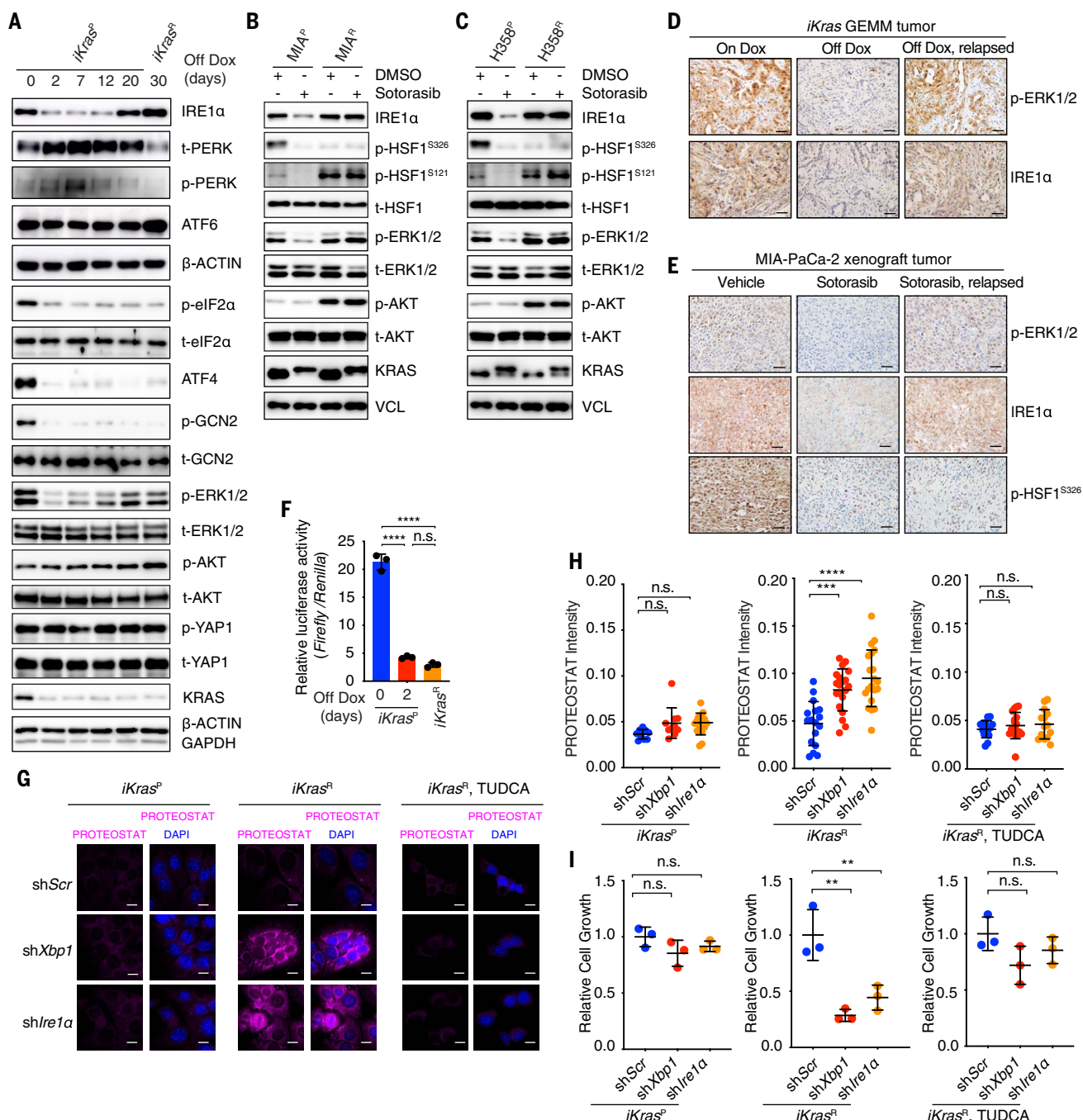


Fig. 2. Oncogenic KRAS inactivation differentially affects the key nodes of the proteostasis regulatory network. (A) Immunoblot with indicated antibodies in whole-cell lysates of *iKras^P* at different time points after *Kras*^{G12D} inactivation through Dox-withdrawal (Off Dox) until the cells acquired resistance to *Kras*^{G12D} inactivation (*iKras^R* cell). (B and C) Immunoblot with indicated antibodies in whole-cell lysates of parental or sotorasib-resistant (B) MIA-PaCa-2 or (C) H358 cells treated with DMSO or 30 nM sotorasib. (D) Immunohistochemical (IHC) staining with indicated antibodies in *iKras* GEMM tumors treated with doxycycline (On Dox), Dox withdrawal for 3 days (Off Dox), or relapsed after 30 weeks of Dox-withdrawal (Off Dox, relapsed). (E) IHC staining with indicated antibodies in MIA-PaCa-2 xenograft tumors treated with vehicle, sotorasib (30mg/kg for 1 day), or relapsed after 9 weeks of sotorasib treatment (30 mg/kg). (F) Relative HSE luciferase activity in *iKras^P* or *iKras^R* cells cultured in the presence or absence of Dox for 2 days. Data are shown as mean ± SD.

n = 3 biological replicates. (G) Representative images and (H) quantification of PROTEOSTAT (magenta) and DAPI (blue) staining in *iKras^P* or *iKras^R* cells infected with lentiviruses encoding scramble short hairpin RNA (shRNA), *Xbp1* shRNA (sh*Xbp1*), or *ire1α* shRNA (sh*ire1α*). Cells were treated with 2.5 mM TUDCA dissolved in water for 2 days as indicated. Data represent the average fluorescence intensity of PROTEOSTAT per cell from each image acquired and presented as mean ± SD from *n* = 10 (On Dox), *n* = 17 (Off Dox), or *n* = 17 (Off Dox + TUDCA) images. (I) CCK-8 assay was used to quantify cell viability of *iKras* cells treated as in (G) and (H). Data are presented as mean ± SD relative to shScr, *n* = 3 biological replicates. Ordinary one-way ANOVA with Dunnett's multiple comparisons test in (H) and (I) and ordinary one-way ANOVA with Tukey's multiple comparisons test in (F) was used to calculate *P* values. n.s., not significant, ***P* < 0.01, ****P* < 0.001, *****P* < 0.0001. Scale bar, (D) and (E), 40 μm; (G) 20 μm.

inhibitor MK2206 had little impact on IRE1 α levels in *iKras* P cells (Fig. 3B). Examination of five additional KRAS-mutant cell lines confirmed that MEK/ERK inhibitors, but not PI3K/AKT inhibitors, reduced IRE1 α protein levels (fig. S6, A to C). These effects were similar to what was observed in response to the genetic or pharmacological inhibition of oncogenic KRAS (Fig. 3F and fig. S6D). Recent studies show that SHP2 (SH2 containing protein tyrosine phosphatase-2) is critical for KRAS G12C cycling and ERK activation (30, 33, 66–69). Inhibition of SHP2 with SHP099 substantially suppressed ERK activity and reduced IRE1 α levels in KRAS G12C -mutant H358 cells (fig. S6E), whereas modest effect was observed in KRAS G12D -mutant *iKras* cells because of the limited intrinsic guanosine triphosphatase (GTPase) activity of KRAS G12D (fig. S6F). SHP099 also inhibited the growth of sotorasib-resistant H358 R cells and MIA-PaCa-2 R cells (fig. S6, G and H). Long-term treatment of H358 cells with SHP099 led to drug resistance and recovered proteostasis (fig. S6, I to K), accompanied with IRE1 α restoration in the resistant cells (fig. S6L). Depletion of IRE1 α in SHP2i-resistant cells resulted in marked protein aggregation and resensitized the cells to SHP099 (fig. S6, M to O). Another upstream activator of RAS signaling is epidermal growth factor receptor (EGFR); suppression of EGFR with gefitinib markedly reduced ERK and IRE1 α levels in H358 cells (fig. S6P). By contrast, inhibition of MEK/ERK in non-malignant BEAS-2B lung epithelial cells with nononcogenic RAS signaling barely affected IRE1 α levels (fig. S6, Q and R). Using tissue microarrays, we found that IRE1 α levels correlated with phospho-ERK levels in treatment-naive PDAC patient samples (Fig. 3, C and D), and high expression of IRE1 α was associated with higher histologic tumor grade (Fig. 3E). Collectively, these data demonstrate that oncogenic KRAS-mediated MAPK pathway activation leads to the activation of IRE1 α in parental KRAS-mutant cancers.

MAPK promotes IRE1 α protein stability by inhibiting SEL1L/HRD1-mediated IRE1 α ubiquitination

Sotorasib treatment did not down-regulate IRE1 α mRNA levels (fig. S7A), but it considerably reduced IRE1 α protein abundance in H358 cells (Fig. 3F). Treatment with the proteasome inhibitor MG132 rescued both sotorasib- and trametinib-induced reductions in IRE1 α protein levels in H358 cells (Fig. 3F). Similarly, the observed reduction in IRE1 α protein levels in response to *Kras* G12D inactivation, trametinib, or SCH772984 treatment could be rescued by MG132 in *iKras* P cells (fig. S7, B and C). These data demonstrate that the inhibition of oncogenic KRAS or MAPK promotes proteasome-mediated IRE1 α degradation in parental KRAS-mutant cancers.

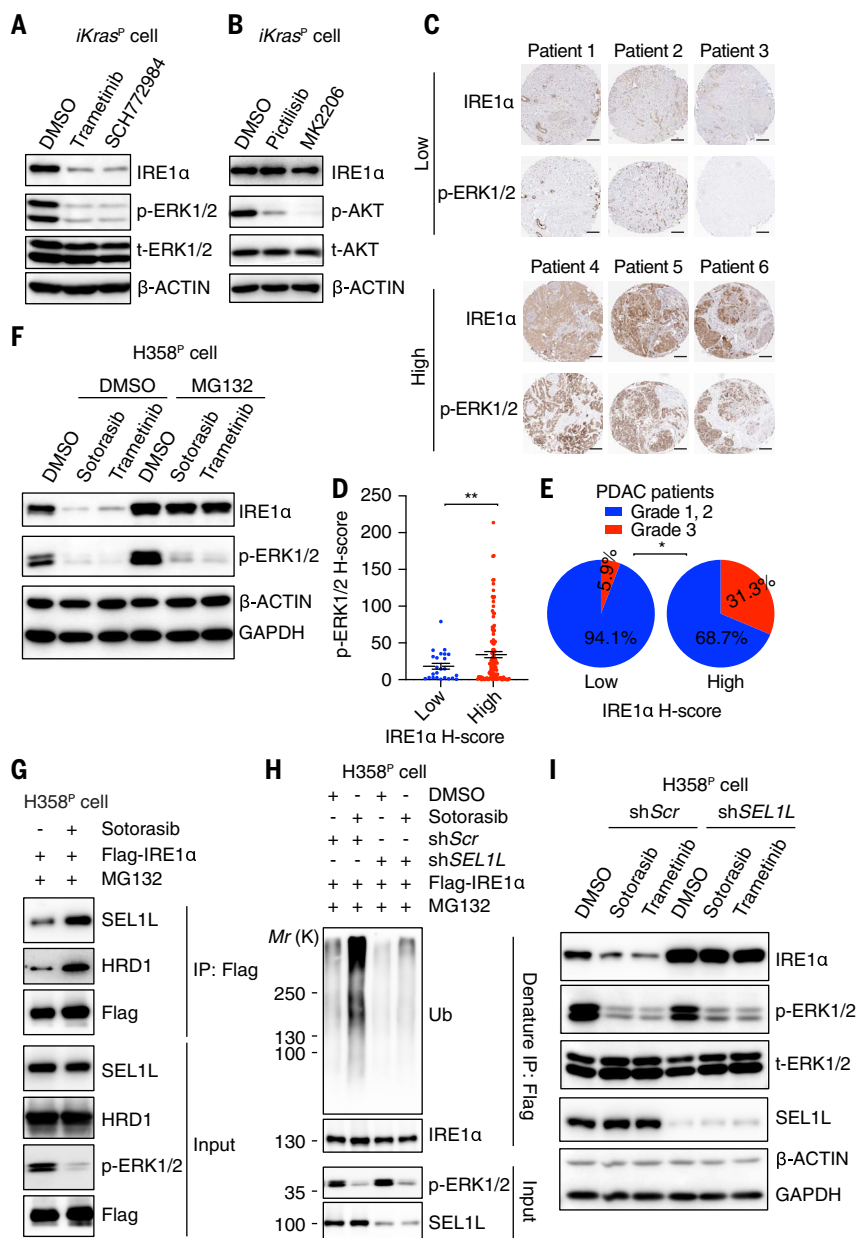


Fig. 3. KRAS-MAPK signaling stabilizes IRE1 α through inhibiting SEL1L-HRD1 mediated IRE1 α ubiquitination. (A and B) Immunoblot with indicated antibodies in whole-cell lysates of *iKras* P cells treated with DMSO, trametinib (MEK inhibitor; 20 nM), SCH772984 (ERK inhibitor; 1 μ M), pictilisib (PI3K inhibitor; 1 μ M), or MK2206 (AKT inhibitor; 2 μ M) as indicated for 2 days. (C) Representative images of IHC staining of IRE1 α and p-ERK1/2 in tissue microarray of treatment naive tumors from PDAC patients. Scale bar, 200 μ m. (D) H-score of p-ERK1/2 in tissue microarray samples with distinct IRE1 α intensities. Data are presented as mean \pm SEM. (E) Proportion of patients with different tumor grades in PDAC patients with low or high IRE1 α H-score. (F) Immunoblot with indicated antibodies in whole-cell lysates of H358 P cells treated with DMSO, 30 nM sotorasib, or 20 nM trametinib for 2 days. Cells were treated with DMSO or 1 μ M MG132 for 12 hours before harvest. (G) Sotorasib promotes the interaction between IRE1 α and SEL1L/HRD1. H358 P cells expressing Flag-IRE1 α were treated with DMSO or 30 nM sotorasib for 2 days and subjected to immunoprecipitation (IP) with anti-Flag M2 agarose beads. (H) Sotorasib promotes SEL1L-dependent IRE1 α ubiquitination. H358 P cells expressing Flag-IRE1 α and shScr or shSEL1L were treated with DMSO or 30 nM sotorasib for 2 days and subjected to denature IP with anti-Flag M2 agarose beads. The immunoblot was probed with antibody to ubiquitin (Ub) to detect IRE1 α ubiquitination. In (G) and (H), MG132 (1 μ M) was added into the culture medium 12 hours before harvest. (I) Immunoblot with indicated antibodies in whole-cell lysates of H358 P cells infected with lentiviruses encoding shScr or shSEL1L and treated with DMSO, 30 nM sotorasib, or 20 nM trametinib for 2 days. Two-tailed, unpaired Student's *t* test with Welch's correction in (D) and Fisher's exact test in (E) was used to calculate *P* values. **P* < 0.05, ***P* < 0.01.

IRE1 α is a bona fide substrate of the SEL1L/HRD1 ER-associated degradation (ERAD) complex (70), which is composed of the E3 ubiquitin ligase HRD1 and its adapter protein SEL1L (suppressor/enhancer of lin-12-like) (71). The SEL1L/HRD1 complex ubiquitinates and targets IRE1 α for proteasomal degradation in multiple cell types (70, 72, 73). Sotorasib treatment substantially enhanced the association between IRE1 α and the SEL1L/HRD1 complex (Fig. 3G), resulting in increased IRE1 α ubiquitination in H358 cells (Fig. 3H). Sotorasib also promoted the interaction of IRE1 α with p97 and NPL4 (nuclear protein localization protein 4) (fig. S7, D and E), which deliver the ubiquitinated ERAD substrates to the proteasome for degradation (74). SEL1L depletion reduced sotorasib- or trametinib-induced IRE1 α ubiquitination and restored IRE1 α protein levels (Fig. 3, H and I, and fig. S7F), leading to the prevention of KRAS-MAPK inhibition–induced protein aggregation (fig. S7G). Inhibition of p97 with CB5083 (75) also rescued sotorasib-induced IRE1 α degradation (fig. S7I). Consistently, *Selll* or *Hrd1* depletion in *iKras*^P cells blocked the induction of IRE1 α degradation and prevented protein aggregation in response to *Kras*^{G12D} extinction and trametinib or SCH772984 treatment (fig. S7, J to P). These data demonstrate that oncogenic KRAS-mediated MAPK activation stabilizes IRE1 α protein by preventing SEL1L/HRD1-mediated ubiquitination and subsequent proteasomal degradation.

ERK directly interacts with and phosphorylates IRE1 α

Oncogenic KRAS-MAPK did not directly regulate ERAD complex expression in *iKras*^P or H358 cells (Fig. 3I and fig. S7, J, M, and Q). It is well established that phosphorylation often interferes with protein-protein interactions and thus regulates protein ubiquitination and stability. We tested whether MAPK might promote IRE1 α phosphorylation, resulting in IRE1 α disassociation from the SEL1L/HRD1 complex. The expression of a constitutively activated MEK construct (MEK^{DD}) dramatically enhanced IRE1 α phosphorylation in 293T cells detected with an antibody to phospho-MAPK substrate motif (fig. S8A). By contrast, sotorasib treatment substantially reduced IRE1 α phosphorylation levels compared with control H358 cells (Fig. 4A). Co-immunoprecipitation (co-IP) assay demonstrated that ERK interacted with IRE1 α in 293T cells and H358 cells (Fig. 4B and fig. S8B). Furthermore, glutathione *S*-transferase (GST) pull-down and in vitro kinase assays confirmed that both ERK1 and ERK2 directly interacted with and phosphorylated IRE1 α in vitro (Fig. 4, C and D, and fig. S8, C to H). Depletion of *ERK1* or *ERK2* in H358 cells revealed that both ERK1 and ERK2 regulated IRE1 α phosphorylation (fig. S8I). IRE1 α possesses three putative ERK binding D-motifs

(Fig. 4E) (76). Deletion of the D-motif at amino acids 687 to 701 largely disrupted the binding between ERK and IRE1 α (fig. S8J). Collectively, these data demonstrate that ERK directly interacts with and phosphorylates IRE1 α .

Sequence analysis showed that human IRE1 α contains four putative ERK phosphorylation sites at Ser⁵²⁵ (S525), Ser⁵²⁹ (S529), Ser⁵⁴⁹ (S549), and Thr⁹⁷³ (T973), which is consistent with the minimal ERK substrate motif pS/T*P (Fig. 4E). Mass spectrometry analysis of IRE1 α protein purified from control or MEK^{DD}-expressing 293T cells confirmed the ERK-dependent phosphorylation of IRE1 α at S525, S529, S549, and T973 (fig. S9, A to C). We mutated the identified phospho-serine or -threonine amino acids to alanine (A) and performed an in vitro kinase assay using [γ -³²P] adenosine 5'-triphosphate (ATP). The kinase-dead form of IRE1 α ^{K599A} was used as a backbone to exclude the effects of IRE1 α autop phosphorylation. ERK was able to directly phosphorylate kinase-dead autophosphorylation-deficient IRE1 α ^{K599A} (Fig. 4F). The T973A mutation (in which threonine was replaced with alanine at position 973) markedly reduced but did not eliminate ERK-dependent IRE1 α ^{K599A} phosphorylation (Fig. 4F). Additional mutation of S525, S529, or S549 to A together with T973A further decreased the IRE1 α phosphorylation (Fig. 4F). The simultaneous mutation of all four sites largely abolished the ERK-dependent IRE1 α ^{K599A} phosphorylation (Fig. 4F). In agreement, mutation of these four S or T to A (designated as 4A mutant) diminished ERK-dependent phosphorylation on WT IRE1 α (Fig. 4G and fig. S9D). The IRE1 α mutations did not affect IRE1 α binding with ERK (fig. S9, D and E). Collectively, these data identify S525, S529, S549, and T973 as ERK phosphorylation sites on IRE1 α . Analysis of Clinical Proteomic Tumor Analysis Consortium (CPTAC) datasets in patients with NSCLC (77) showed a statistically significant correlation between IRE1 α -S549 phosphorylation and ERK phosphorylation in treatment-naïve NSCLC patients (Fig. 4H and fig. S9F). The peptides containing S525, S529, and T973 were not covered in the CPTAC datasets and could not be evaluated in patients.

To determine the functional relevance of IRE1 α phosphorylation sites, we generated a loss-of-function mutation for each site. Single-site mutation was insufficient to promote IRE1 α interaction with HRD1 and did not alter IRE1 α levels in *iKras* cells (Fig. 4, I and J). Simultaneous mutation of all four sites promoted IRE1 α interaction with HRD1 and its degradation (Fig. 4, I and J). In vitro pull-down assays confirmed that ERK-mediated IRE1 α phosphorylation reduced IRE1 α interaction with HRD1/SEL1L and that phospho-deficient IRE1 α ^{4A} mutant bound to HRD1 regardless of ERK presence (fig. S10, A to E). By contrast, gain-of-function phosphomimetic mutation for each

individual site (S525D, S529D, S549D, or T973E, where D is aspartate and E is glutamate) disrupted IRE1 α interaction with HRD1 (Fig. 4K), leading to the stabilization of IRE1 α protein in the absence of ERK (Fig. 4L). Similar effects were observed for IRE1 α ^{SDTE} mutant with gain-of-function mutation for all four sites (Fig. 4, K and L, and fig. S10F). IRE1 α ^{SDTE} was resistant to sotorasib- or SCH772984-promoted protein degradation in MIA-PaCa-2 cells (fig. S10, G and H). As a result, sotorasib failed to induce protein aggregation in IRE1 α ^{SDTE}-expressing MIA-PaCa-2 tumors (Fig. 5, A to C). These tumors became partially resistant to sotorasib-induced antitumor effects (Fig. 5D). In line with these data, the IRE1 α ^{SDTE} mutant rescued IRE1 α depletion-induced protein aggregation, phospho-ERK, and cell growth defects in *iKras*^R cells (fig. S10, I to L). Single-site phospho-deficient IRE1 α mutant also rescued these phenotypes owing to the presence of the other three phosphorylated sites (fig. S10, L to O). The phospho-deficient IRE1 α ^{4A} mutant failed to restore IRE1 α protein levels and was unable to rescue these phenotypes (fig. S10, L to O). Collectively, these data demonstrate that IRE1 α phosphorylation at S525, S529, S549, and T973 inhibits IRE1 α association with the ERAD complex, leading to enhanced stability, maintaining proteostasis.

A screen of 32 serine and threonine phosphatases in 293T cells revealed that expression of SCP3 substantially reduced MEK^{DD}-induced IRE1 α phosphorylation (fig. S11, A to C). In vitro phosphatase assays and co-IP experiments confirmed that SCP3 interacted with and directly dephosphorylated IRE1 α (Fig. 5E, and fig. S11D). *Scp3* silencing increased IRE1 α phosphorylation, and overexpression of SCP3 reduced IRE1 α phosphorylation, in *iKras* cells (Fig. 5, F and G). Similarly, *SCP3* deletion slowed down sotorasib-induced IRE1 α dephosphorylation in H358 cells (fig. S11E). These data identified SCP3 as the phosphatase regulating IRE1 α phosphorylation, although KRAS did not directly alter SCP3 levels or activities (fig. S11, F to I). Collectively, these analyses establish a mechanism of IRE1 α regulation by oncogenic KRAS.

Multiple pathways converge to reactivate IRE1 α in KRASⁱ-resistant cancer cells

Next, we sought to determine how IRE1 α evades oncogenic KRAS inhibition and determine the reactivation mechanism in KRASⁱ-resistant cells. Oncogenic KRAS was efficiently suppressed by Dox withdrawal in *iKras*^R cells (Fig. 2A and fig. S1B), and most KRAS proteins were bound by sotorasib in sotorasib-resistant H358 (*H358*^R) and MIA-PaCa-2 (MIA-PaCa-2^R) cells, similar to observations of parental cells (Fig. 2, B and C). Furthermore, silencing of KRAS in *H358*^R cells did not hinder IRE1 α reactivation (fig. S12A). These data exclude the possibility that the inefficient inhibition of oncogenic KRAS drives IRE1 α reactivation in these

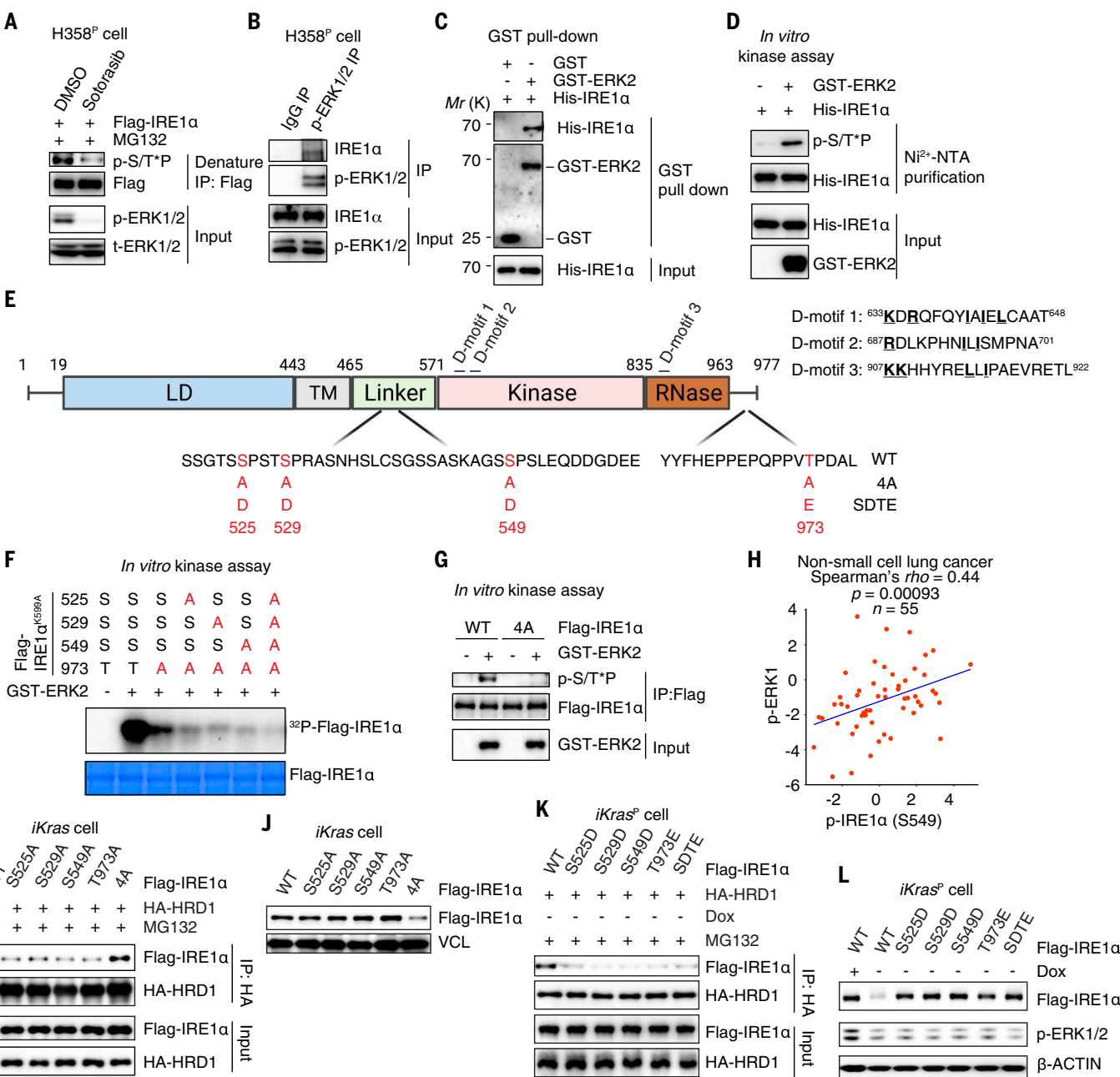


Fig. 4. ERK directly phosphorylates and stabilizes IRE1 α . (A) H358^P cells expressing Flag-IRE1 α were treated with DMSO or 30 nM sotorasib for 2 days and subjected to denature IP with anti-Flag M2 agarose beads. The immunoblot was probed with anti-phospho-MAPK substrates motif (S/T*P) antibody (p-S/T*P) to detect IRE1 α phosphorylation. (B) Whole-cell lysate of H358^P cells were subjected to co-IP with rabbit anti-p-ERK1/2 antibody or normal rabbit immunoglobulin G (IgG). (C) GST pull-down assay was performed by using recombinant His-tagged IRE1 α and GST-ERK2 protein. (D) In vitro kinase assay was performed by using recombinant GST-ERK2 and His-IRE1 α . After phosphorylation reaction, the proteins were denatured with 8M urea buffer and subjected to purification of His-IRE1 α with Ni²⁺-NTA agarose to detect IRE1 α phosphorylation by use of anti-p-S/T*P antibody. (E) Schematic illustration of human IRE1 α protein domains, three putative ERK binding D-motifs, and ERK phosphorylation sites at Ser⁵²⁵, Ser⁵²⁹, Ser⁵⁴⁹, and Thr⁹⁷³ (red). Phospho-deficient (4A) and

phospho-mimetic (SDTE) mutations of IRE1 α are shown. LD, luminal domain; TM, transmembrane domain. (F) In vitro [γ -³²P] ATP kinase assay by using different Flag-tagged IRE1 α mutants and GST-ERK2. The IRE1 α phosphorylation was detected with autoradiography. One-Step Blue Protein Stain (Biotium) was used to detect IRE1 α protein loading. (G) In vitro kinase assay by using equal amount of Flag-tagged WT or phospho-deficient IRE1 α mutant proteins (4A) and GST-ERK2. (H) Spearman correlation between p-IRE1 α (at S549) and p-ERK1 (at Y204) in 55 patients with NSCLC. (I and K) Whole-cell lysates of iKras cells expressing HA-HRD1 together with WT or mutant IRE1 α cultured in the absence of Dox were subjected to IP with anti-HA agarose beads to detect IRE1 α interaction with HRD1. In (A), (I), and (K), MG132 (1 μ M) was added into the culture medium 12 hours before harvest. (J and L) Immunoblot of WT or mutant IRE1 α in whole-cell lysates of iKras cells cultured in the presence or absence of Dox for 2 days.

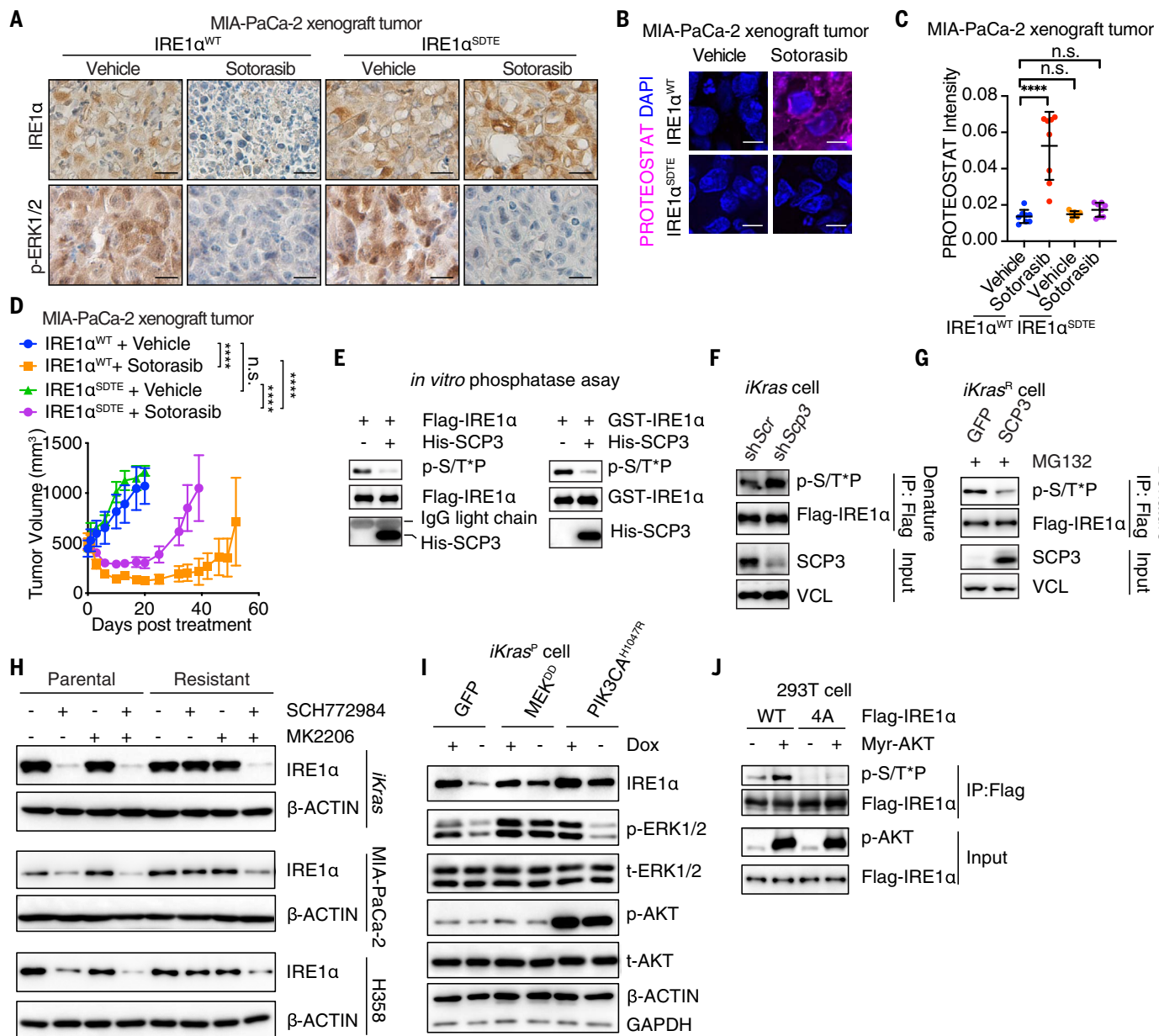


Fig. 5. Multiple pathways converge to restore IRE1 α in KRASi-resistant cancer cells. (A) IHC staining of p-ERK1/2 and IRE1 α in shRNA-resistant IRE1 α^{WT} - or IRE1 α^{SDTE} -transduced, endogenous IRE1 α -depleted MIA-PaCa-2 tumors treated with vehicle or sotorasib (100 mg/kg) for 4 days. Scale bar, 40 μ m. (B) Representative images and (C) quantification of PROTEOSTAT (magenta) and DAPI (blue) staining in MIA-PaCa-2 tumors as in (A). Data represent average fluorescence intensity of PROTEOSTAT per cell from each image acquired and are presented as mean \pm SD from $n = 8$ independent images. Scale bar, 20 μ m. (D) Tumor volume quantification of MIA-PaCa-2 tumors as in (A). (E) In vitro phosphatase assay. (Left) Phosphorylated Flag-IRE1 α protein purified from MEK^{DD}-expressing 293T cells or (right) recombinant IRE1 α protein phosphorylated by recombinant ERK2 in vitro were subjected to in vitro phosphatase assay with recombinant SCP3. (F and G) iKras cells expressing Flag-IRE1 α were infected with shRNA targeting (F) Scr or Scp3 and (G) GFP- or

SCP3-expressing lentivirus. The whole-cell lysates were subjected to denature IP with anti-Flag M2 agarose beads, followed by immunoblot with antibody to pS/T*P to detect IRE1 α phosphorylation. (H) Immunoblot of IRE1 α in whole-cell lysates of parental and KRAS inhibition-resistant cells treated with DMSO, 2 μ M MK2206, and/or 1 μ M SCH772984 for 2 days (MIA-PaCa-2 and H358 cells) or 14 days (iKras cells). (I) Immunoblot of IRE1 α in whole-cell lysates of iKras^P cells expressing GFP, MEK^{DD}, or PIK3CA^{H1047R} in the presence or absence of Dox for 2 days. (J) 293T cells expressing IRE1 α^{WT} or IRE1 α^{4A} in the presence or absence of myr-AKT were subjected to IP with anti-Flag M2 agarose beads followed by immunoblot to detect IRE1 α phosphorylation. Ordinary one-way ANOVA with Dunnett's multiple comparisons test in (C) and two-way ANOVA with Bonferroni's multiple comparisons test in (D) were used to calculate P values. n.s., not significant; **P < 0.01, ***P < 0.001, ****P < 0.0001.

resistant cells. eIF2 α phosphorylation inhibits global protein synthesis (61, 78). Consistent with the inactivated phospho-eIF2 α in KRASi-resistant cells (Fig. 2A), we observed increased global protein synthesis in iKras^R cells evidenced by

enhanced puromycin incorporation compared with that in iKras^P cells (fig. S12B). However, inhibition of protein synthesis with cycloheximide did not affect IRE1 α /XBPI in iKras^R cells (fig. S12, C and D). Furthermore, ER stress

sensing-deficient IRE1 $\alpha^{Δ2M}$ mutant (79) was similarly restored in KRASi-resistant cells as that of WT IRE1 α (fig. S12, E and F) and successfully rescued IRE1 α depletion-induced phenotypes (fig. S12, G to J). These data

demonstrate that IRE1 α is reactivated in KRAS i -resistant cells in an ER stress-independent manner.

Recent studies report reactivated ERK and AKT as sotorasib-resistant mechanisms in patients (18, 19, 21–23). We observed the reactivation of phospho-ERK and the hyperactivation of phospho-AKT in sotorasib-resistant MIA-PaCa-2 R and H358 R cells compared with their respective parental cells (Fig. 2, B and C). Unexpectedly, the inhibition of reactivated ERK through SCH772984 treatment was insufficient to suppress IRE1 α levels in MIA-PaCa-2 R , H358 R , and *iKras* R cells (Fig. 5H) as well as in MIA-PaCa-2 R and *iKras* R tumors *in vivo* (fig. S13, A and B). Similarly, the suppression of AKT through MK2206 treatment had no effect on IRE1 α levels in KRAS i -resistant cells (Fig. 5H). However, the simultaneous suppression of both ERK and AKT successfully blunted IRE1 α reactivation in MIA-PaCa-2 R , H358 R , and *iKras* R cells (Fig. 5H) and in MIA-PaCa-2 R and *iKras* R tumors *in vivo* (fig. S13, A and B). Consistently, the hyperactivation of either the MEK/ERK pathway, through expression of MEK DD , or the PI3K/AKT pathway, through the expression of constitutively active PIK3CA $H1047R$ or myr-AKT, resulted in IRE1 α restoration in the absence of oncogenic KRAS in *iKras* cells (Fig. 5I and fig. S13C). myr-AKT also promoted WT, but not phospho-deficient 4A mutant, IRE1 α phosphorylation at serine and threonine residues (Fig. 5J), suggesting that these phosphorylation sites are regulated by both ERK and hyperactivated AKT in KRAS i -resistant cells. In agreement, either the activation of MEK/ERK, through MEK DD expression, or the hyperactivation of AKT, through myr-AKT expression, was sufficient to disrupt the interaction of the SEL1L/HRD1 E3 ligase complex with IRE1 α (fig. S13D). By contrast, the simultaneous suppression of both ERK and AKT, but not ERK or AKT alone, promoted IRE1 α interaction with the SEL1L/HRD1 E3 ligase complex in sotorasib-resistant MIA-PaCa-2 R cells (fig. S13E). Yes-associated protein 1 (YAP1) also drives resistance of certain tumors to KRAS i (37, 38). However, deletion of YAP1 in *iKras* R -YAP1 cells derived from YAP1-amplified GEMM tumors escaping KRAS $G12D$ addiction did not affect IRE1 α and proteostasis (fig. S14, A to F). Instead, IRE1 α and proteostasis were dependent on ERK and AKT in these cells despite reduced ERK activity compared with that in parental *iKras* cells (fig. S14, G to J). Collectively, these data demonstrate that both reactivated ERK and hyperactivated AKT converge through IRE1 α phosphorylation at S525, S529, S549, and T973 to prevent ubiquitination-mediated proteasomal degradation of IRE1 α in KRAS i -resistant cancer cells. Blocking either individual pathway is not sufficient to inhibit IRE1 α because of functional redundancy and compensation by the other pathway.

Next, we sought to understand the mechanism that activates ERK and AKT in the KRAS i -resistant cells. Receptor tyrosine kinases (RTKs) activation is one of the most common mechanisms driving sotorasib resistance in patients (20–22), and RTKs are known to activate ERK and AKT (17, 19, 30, 80). Array analysis of 49 RTKs in parental and sotorasib-resistant H358 and MIA-PaCa-2 models revealed the induction of multiple and distinct sets of RTKs in each model (fig. S15, A, B, and E). In the H358 model, EGFR, ErbB2, ErbB3, fibroblast growth factor receptor 3 (FGFR3), and vascular endothelial growth factor receptor 2 (VEGFR2) were substantially induced in the resistant cells (fig. S15, A and B). Inhibiting these RTKs with combined sapitinib, AZD4547, and axitinib, but not individual inhibitor alone, completely suppressed ERK reactivation in H358 R cells (fig. S15, C and D). Blocking FGFR3 with AZD4547 largely abolished AKT hyperactivation (fig. S15, C and D). These up-regulated RTKs had to be simultaneously suppressed to completely blunt both ERK and AKT, resulting in the abrogation of IRE1 α restoration in H358 R cells (fig. S15D). Similar to the H358 model, blocking multiple, but not individual, up-regulated RTKs [including EGFR, ErbB2, VEGFR, platelet-derived growth factor receptor β (PDGFR β), and discoidin domain receptor 2 (DDR2)] completely suppressed both ERK and AKT, leading to the abrogation of IRE1 α restoration in a MIA-PaCa-2 R cell (fig. S15, F and G). Treatment of MIA-PaCa-2 R tumors with combined RTK inhibitors—including sapitinib, axitinib, and VU6015929—confirmed the inactivation of ERK and AKT *in vivo*, leading to the suppression of IRE1 α , marked induction of protein aggregation, and reduced tumor growth (fig. S15, H to K). However, they were not well tolerated in the tumor-bearing mice, causing rapid drop of body weight and early lethality (fig. S15L). Collectively, these data demonstrate that multiple and diverse sets of RTKs drive ERK and AKT activation in different KRAS i -resistant tumors, which subsequently converge on IRE1 α to reestablish proteostasis.

IRE1 α inhibition sensitizes oncogenic KRAS-driven tumors to a MEK inhibitor

Although the simultaneous suppression of the MAPK and PI3K pathways, or diverse upstream RTKs, effectively inhibits IRE1 α , the heterogeneous resistance mechanisms in different patients (18–23) and dose-limiting, on-target toxicity of these inhibitors (81, 82) limit their clinical applications for intervening in IRE1 α -mediated proteostasis reprogramming in treatment-resistant tumors. Therefore, we directly targeted the IRE1 α /XBPI pathway in KRAS-driven cancers in combination with KRAS $G12C$ or MEK inhibitor. Although MEK inhibitor trametinib or *Xbp1* deletion alone both modestly impeded *iKras* tumor growth *in vivo*,

the loss of *Xbp1* significantly enhanced the response of *iKras* xenograft tumors to trametinib and induced marked protein aggregation (fig. S16, A to D). Treatment of *iKras* tumors with a highly selective IRE1 α RNase inhibitor, ORIN1001 (83–86), recapitulated the effects of the *Xbp1* deletion and markedly enhanced the sensitivity of the *iKras* tumors to trametinib treatment with significant induction of protein aggregation (fig. S16, A and E to G). In a cohort of PDAC patient-derived xenograft (PDX) models (fig. S16N), ORIN1001 also significantly enhanced the sensitivity of the KRAS $G12D$ -mutant PATC53 (Fig. 6, A to D), PATC148 (Fig. 6E and fig. S16, H and I), PDAC35 (Fig. 6F and fig. S16, J and K), SW1990 (Fig. 6, G and H, and fig. S16, L and M), and KRAS $G12V$ -mutant PDAC19 PDX (Fig. 6I) tumors to trametinib treatment and potently induced protein aggregation in the combination therapy-treated tumors. Collectively, these *in vivo* data demonstrate that IRE1 α /XBPI inhibition dramatically enhanced the response of KRAS-mutant PDAC tumors to trametinib treatment.

IRE1 α inhibition enhances the responses of KRAS $G12C$ -driven tumors to sotorasib

Next, we examined the effects of IRE1 α inhibition on the response to sotorasib treatment in KRAS $G12C$ -driven tumors. *IRE1 α* silencing modestly reduced MIA-PaCa-2 xenograft tumor growth but not to the extent observed with sotorasib treatment (Fig. 7A and fig. S17A). However, IRE1 α deficiency significantly enhanced the response of these tumors to sotorasib treatment and considerably suppressed tumor relapse (Fig. 7A and fig. S17A). By contrast, PERK depletion had little impact on MIA-PaCa-2 tumor growth and response to sotorasib, as well as *IRE1 α* depletion-induced tumor sensitivity to sotorasib (fig. S17, B to E), excluding the involvement of PERK in KRAS i resistance. IRE1 α inhibition with ORIN1001 treatment combined with sotorasib treatment also resulted in complete MIA-PaCa-2 tumor regression and long-term remission (Fig. 7B and fig. S17, F and G). We did not observe significant bodyweight changes or signs of toxicity in the combination treatment group (fig. S17, H and I). Treatment of non-KRAS-addicted MIA-PaCa-2 R tumors with ORIN1001 alone also substantially impeded the tumor growth (Fig. 7C) but did not result in complete response. The reduced efficacy with ORIN1001 alone was likely due to the absence of sotorasib, which was required for long-term inhibition of KRAS $G12C$ (87), and rewiring of the proteostasis network to be IRE1 α -centered.

ORIN1001 has more than 100-fold mammalian enzyme selectivity over its yeast ortholog (83). Structure analysis of the mammalian and yeast enzymes revealed a critical residue, Val⁹¹⁸ (V918), in mammalian IRE1 α that differs from the yeast enzyme and could be critical for ORIN1001 binding (Fig. 7D). Binding of ORIN1001

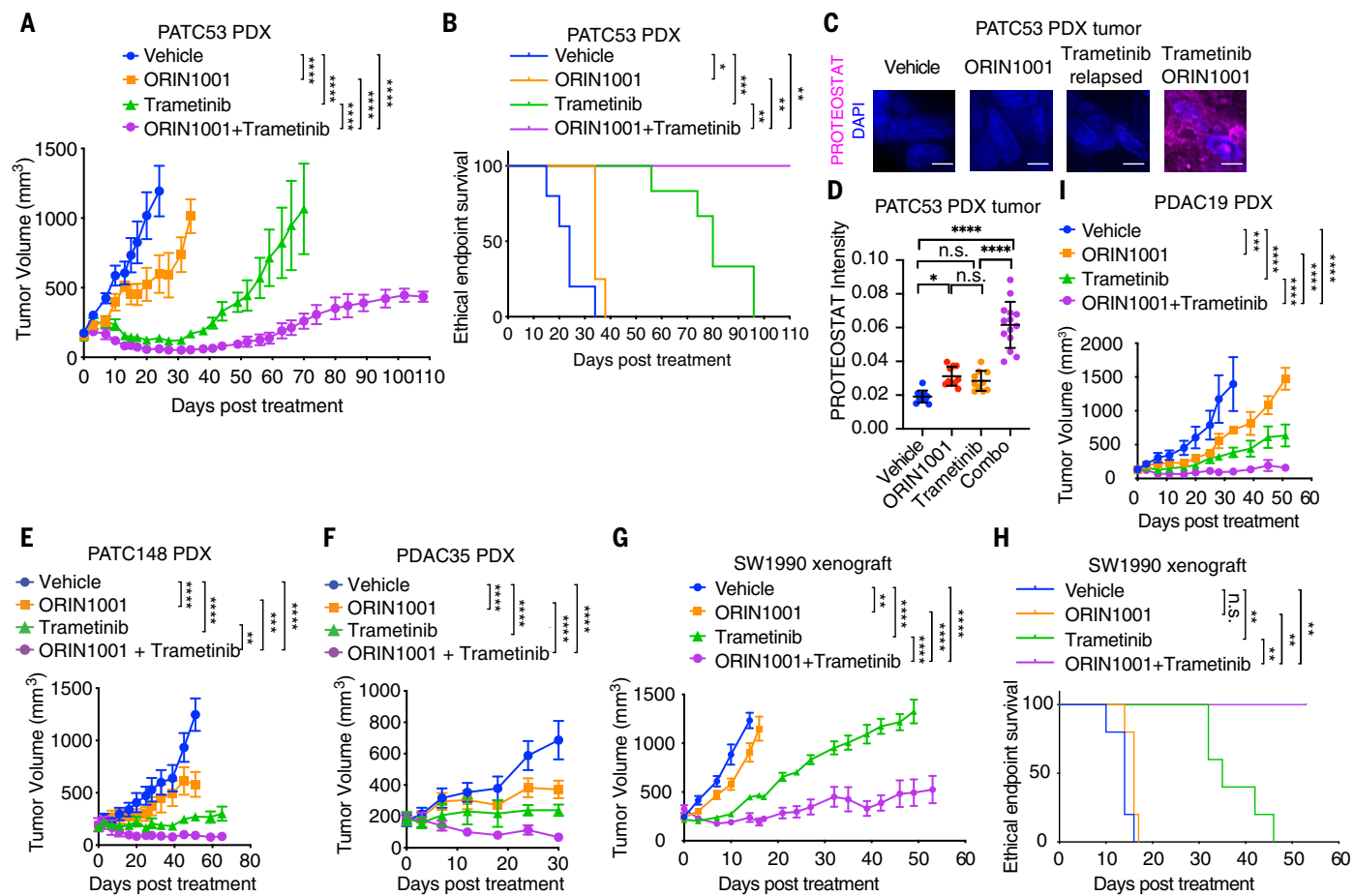


Fig. 6. IRE1 α inhibition sensitizes oncogenic KRAS-driven tumors to MEK inhibition.

(A) Tumor volume quantification of established PATC53 PDX tumors in severe combined immunodeficient (SCID)/beige mice treated with vehicle ($n = 5$ mice), IRE1 α RNase inhibitor ORIN1001 ($n = 4$ mice), MEK inhibitor trametinib ($n = 6$ mice), or ORIN1001 plus trametinib ($n = 4$ mice). **(B)** Kaplan-Meier survival curve of PATC53 PDX tumor-bearing mice under treatment as indicated in (A). **(C)** Representative images and **(D)** quantification of PROTEOSTAT (magenta) and DAPI (blue) staining in endpoint PATC53 xenograft tumors treated as in (A). Data represent average fluorescence intensity of PROTEOSTAT per cell from each image acquired and are presented as mean \pm SD from $n = 10$ independent images. Scale bar, 20 μm . **(E)** Tumor volume quantification of established PATC148 PDX tumors in SCID/beige mice treated with vehicle ($n = 6$ mice), ORIN1001 ($n = 6$ mice), trametinib ($n = 4$ mice), or ORIN1001 plus trametinib ($n = 4$ mice). **(F)** Tumor volume quantification of established PDAC35 PDX tumors in SCID/beige mice treated with vehicle

($n = 5$ mice), ORIN1001 ($n = 4$ mice), MEK inhibitor trametinib ($n = 4$ mice), or ORIN1001 plus trametinib ($n = 4$ mice). **(G)** Tumor volume quantification of established SW1990 PDAC xenograft tumors in SCID/beige mice treated with vehicle ($n = 6$ mice), ORIN1001 ($n = 6$ mice), trametinib ($n = 5$ mice), or ORIN1001 plus trametinib ($n = 4$ mice). **(H)** Kaplan-Meier survival curve of SW1990 PDAC xenograft tumor-bearing mice under treatment as indicated in (G). **(I)** Tumor volume quantification of established PDAC19 PDX tumors in SCID/beige mice treated with vehicle, ORIN1001, trametinib, or ORIN1001 plus trametinib ($n = 4$ mice). ORIN1001, 150 mg/kg; trametinib, 1 mg/kg. Data are presented as mean \pm SEM in (A), (E) to (G), and (I) and mean \pm SD in (D). Two-way ANOVA with Bonferroni's multiple comparisons test in (A), (E) to (G), and (I); log-rank (Mantel-Cox) test in (B) and (H); and ordinary one-way ANOVA with Tukey's multiple comparisons test in (D) was used to calculate P values. n.s., not significant; * $P < 0.05$, ** $P < 0.01$, *** $P < 0.001$, **** $P < 0.0001$.

to IRE1 α results in the formation of an imine that could be reduced and detected with ultraviolet (UV)-excited fluorescence (Fig. 7E). Whereas purified WT IRE1 α protein directly bound to ORIN1001, mutation of valine to phenylalanine at V918 (V918F) abolished the binding (Fig. 7F). The V918F mutation did not affect the ability of ER stressor tunicamycin to induce *XBPI* splicing but completely abolished the response of IRE1 α to ORIN1001 (Fig. 7G). Treatment of IRE1 α ^{V918F}-expressing MIA-PaCa-2^R tumors with ORIN1001 failed to inhibit XBPIs in vivo (Fig. 7H). These data identify IRE1 α ^{V918F}

as a drug-resistant mutant that retains intact RNase activity but is immune to ORIN1001. The IRE1 α ^{V918}-expressing, but not WT IRE1 α -expressing, MIA-PaCa-2^R tumors were completely immune to ORIN1001-induced sensitivity to sotorasib (Fig. 7I) and protein aggregation (Fig. 7J and K). Collectively, these data confirm the on-target effects of ORIN1001 in vivo.

We also tested the therapeutic efficacy of combined ORIN1001 and sotorasib treatment in the H358 NSCLC model. The H358 tumors were highly sensitive to sotorasib treatment, and complete regression was observed within

70 days (Fig. 8A). However, the termination of sotorasib treatment resulted in rapid tumor relapse (Fig. 8A). Tumors treated with combined sotorasib and ORIN1001 did not relapse after treatment termination (Fig. 8, A and B). KRAS-resistance mechanisms are heterogeneous in human patients (18–23). To assess the human relevance, we treated five *KRAS*^{G12C}-mutant NSCLC PDX models with sotorasib and ORIN1001. As shown in Fig. 8, C to G, and fig. S18, A to E, ORIN1001 significantly sensitized all five PDX models to sotorasib. In three PDX models (J000096652, TM00186, and TC303AR), the

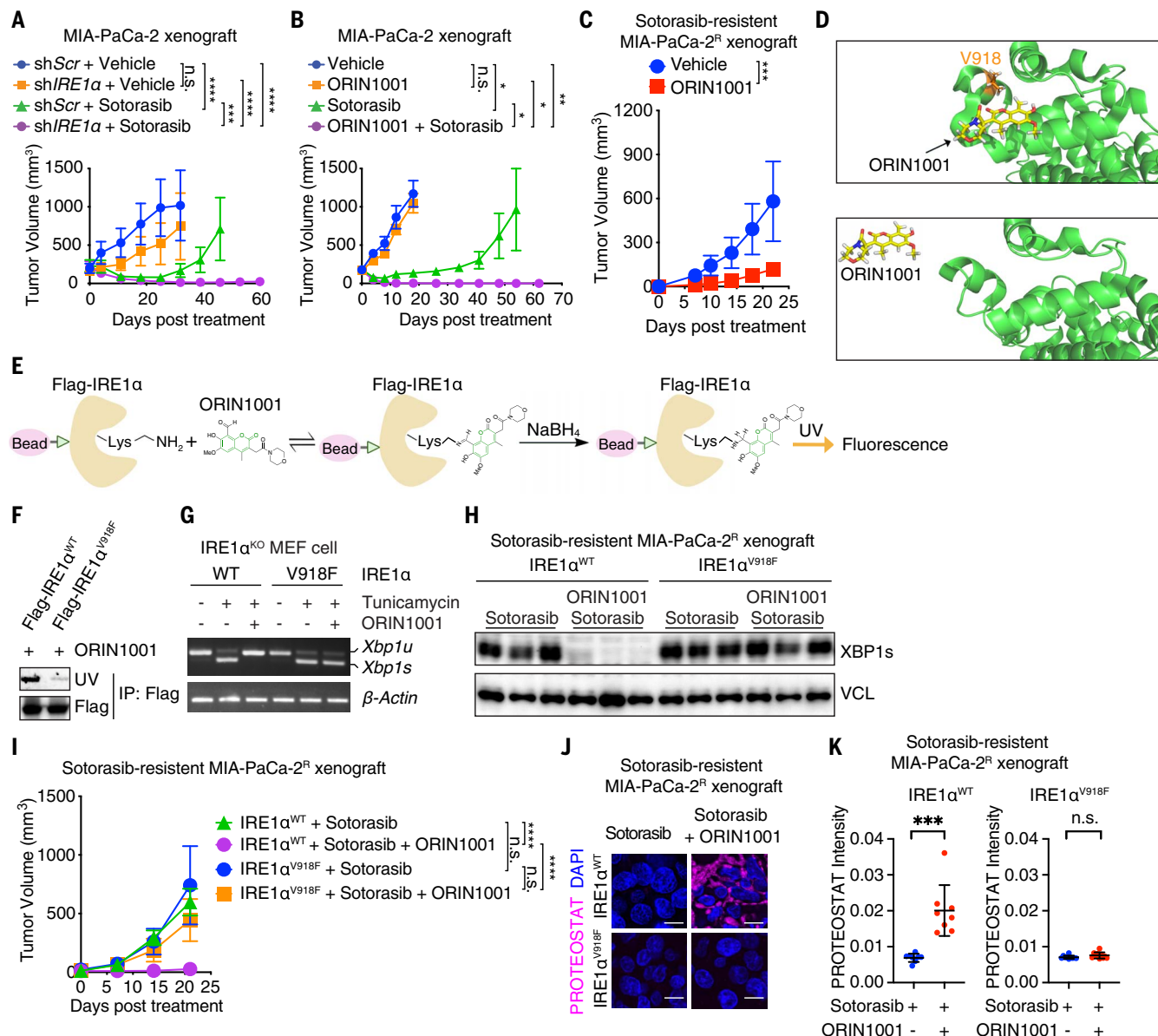


Fig. 7. IRE1 α inhibition enhances tumor responses to sotorasib. (A) Tumor volume of MIA-PaCa-2 tumors transduced with dox-inducible shScr or shIRE1 α and treated with doxycycline water, vehicle ($n = 5$ mice) or sotorasib ($n = 6$ mice). (B) Tumor volume of MIA-PaCa-2 tumors treated with vehicle ($n = 5$ mice), ORIN1001 ($n = 4$ mice), sotorasib ($n = 4$ mice), or both ($n = 5$ mice). (C) Tumor volume of sotorasib-resistant MIA-PaCa-2 R tumors treated with vehicle ($n = 4$ mice) or ORIN1001 ($n = 7$ mice). (D) Docking modeling of ORIN1001 with IRE1 α . V918 is critical for the formation of the shallow pocket at mammalian IRE1 α RNase-active site for ORIN1001 binding. (E) Biochemical fluorescence assay detecting the binding between ORIN1001 and IRE1 α in vitro. (F) Equal amount of Flag-IRE1 α ^{WT} or Flag-IRE1 α ^{V918F} protein purified from 293T cells was used to pull down ORIN1001 in vitro. UV transmission was used to detect ORIN1001 that is covalently bound to IRE1 α protein in the SDS-polyacrylamide gel electrophoresis (SDS-PAGE). (G) Xbp1 splicing in IRE1 α -deleted mouse embryonic fibroblast (MEF) cells expressing

IRE1 α ^{WT} or IRE1 α ^{V918F} and treated with tunicamycin (5 μ g/ml) and/or ORIN1001 (5 μ M) for 6 hours as indicated. (H) Immunoblot of XBP1s in shRNA-resistant IRE1 α ^{WT} or IRE1 α ^{V918F}-transduced, endogenous IRE1 α -depleted MIA-PaCa-2 R tumors treated as indicated. (I) Tumor volume of established shRNA-resistant IRE1 α ^{WT}- or IRE1 α ^{V918F}-expressing, endogenous IRE1 α -depleted, sotorasib-resistant MIA-PaCa-2 R tumors treated as indicated ($n = 10$ mice). (J) Representative images and (K) quantification of PROTEOSTAT and DAPI staining in MIA-PaCa-2 R tumors treated as in (I). Data represent average fluorescence intensity of PROTEOSTAT per cell from each image and are presented as mean \pm SD from $n > 10$ independent images. Scale bar, 20 μ m. Sotorasib, 100 mg/kg; ORIN1001, 300 mg/kg. Data are presented as mean \pm SEM in (A) to (C), and (I). Two-way ANOVA test with Bonferroni's multiple comparisons test in (A) to (C), and (I) and two-tailed, unpaired Student's *t* test in (K) was used to calculate *P* values. n.s., not significant; **P* < 0.05, ***P* < 0.01, ****P* < 0.001, *****P* < 0.0001.

tumors were initially sensitive to sotorasib treatment, but eventually all of the tumors relapsed. Addition of ORIN1001 to sotorasib led to complete responses and prevented tumor re-

lapse (Fig. 8, C to E). In the other two PDX models (J000093018 and TM00192), ORIN1001 also significantly enhanced the tumor responses to sotorasib, but the responses were not as

striking as the other models (Fig. 8, F and G). Analysis of these five PDX models showed that sotorasib did not effectively inhibit MAPK in the J000093018 and TM00192 PDX models

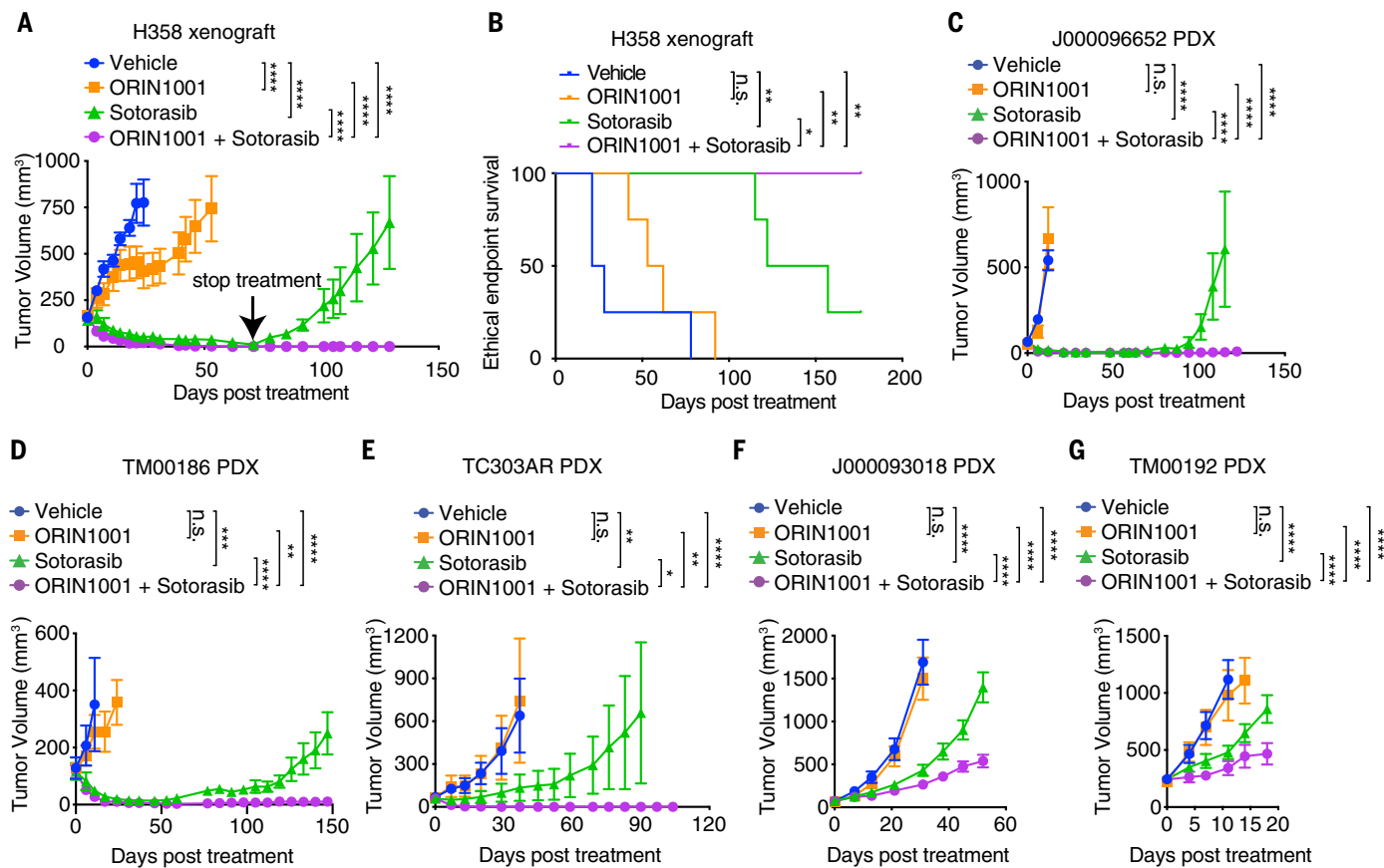


Fig. 8. IRE1 α inhibition enhances the response of KRAS G^{12C} -driven tumors to sotorasib. (A) Tumor volume quantification of established H358 tumors in SCID/beige mice treated with vehicle, ORIN1001, sotorasib, or ORIN1001 plus sotorasib ($n = 4$ mice). Treatment was stopped at day 71. (B) Kaplan-Meier survival curve of H358 tumor-bearing mice under different treatments as indicated in (A) from treatment start time. (C) Tumor volume quantification of established J000096652 PDX tumors in NSG mice treated with vehicle ($n = 6$ mice), ORIN1001 (300 mg/kg; $n = 4$ mice), sotorasib (100 mg/kg; $n = 7$ mice), or ORIN1001 plus sotorasib ($n = 8$ mice). Treatment was stopped at day 65. (D) Tumor volume quantification of established TM00186 PDX tumors in NSG mice treated with vehicle ($n = 6$ mice), ORIN1001 (300 mg/kg; $n = 6$ mice), sotorasib (100 mg/kg; $n = 7$ mice), or ORIN1001 plus sotorasib ($n = 9$ mice). (E) Tumor volume quantification of established TC303AR PDX tumors in NSG mice treated with vehicle ($n = 6$ mice), ORIN1001 (300 mg/kg; $n = 6$ mice), sotorasib (100 mg/kg; $n = 9$ mice), or ORIN1001 plus sotorasib ($n = 9$ mice). Data are presented as mean \pm SEM in (A) and (C) to (G). Two-way ANOVA test with Bonferroni's multiple comparisons test in (A) and (C) to (G) and log-rank (Mantel-Cox) test in (B) was used to calculate P values. n.s., not significant; * $P < 0.05$, ** $P < 0.01$, *** $P < 0.001$, **** $P < 0.0001$.

mice treated with vehicle ($n = 5$ mice), ORIN1001 (300 mg/kg; $n = 5$ mice), sotorasib (100 mg/kg; $n = 9$ mice), or ORIN1001 plus sotorasib ($n = 9$ mice). Treatment was stopped at day 53. (F) Tumor volume quantification of established J000093018 PDX tumors in NSG mice treated with vehicle ($n = 6$ mice), ORIN1001 (300 mg/kg; $n = 6$ mice), sotorasib (100 mg/kg; $n = 9$ mice), or ORIN1001 plus sotorasib ($n = 9$ mice). (G) Tumor volume quantification of established TM00192 PDX tumors in NSG mice treated with vehicle ($n = 6$ mice), ORIN1001 (300 mg/kg; $n = 5$ mice), sotorasib (100 mg/kg; $n = 9$ mice), or ORIN1001 plus sotorasib ($n = 9$ mice). Data are presented as mean \pm SEM in (A) and (C) to (G). Two-way ANOVA test with Bonferroni's multiple comparisons test in (A) and (C) to (G) and log-rank (Mantel-Cox) test in (B) was used to calculate P values. n.s., not significant; * $P < 0.05$, ** $P < 0.01$, *** $P < 0.001$, **** $P < 0.0001$.

(fig. S18, F to J), leading to incomplete reprogramming of the proteostasis network and reduced efficacy (fig. S18, K and L). Collectively, these *in vivo* data demonstrate that IRE1 α inhibition is effective in enhancing the response of KRAS G^{12C} -driven tumors to sotorasib. Combination therapy with ORIN1001 and sotorasib achieves complete responses and prevents tumor relapse in a significant portion of KRAS G^{12C} -driven tumors.

Concluding remarks

Most cancers require a balanced proteostasis network to maintain oncogenic growth. Therapeutic insults often disrupt proteostasis and induce proteotoxic stresses (88). How proteostasis network is orchestrated by driver oncogenes and the proteostasis reprogramming

mechanisms that bypass oncogene addiction and allow for acquired resistance to targeted therapies remain largely unknown. We have shown that oncogenic KRAS is critical for protein quality control in tumor cells. Inhibition of oncogenic KRAS inactivates both cytosolic and ER protein quality control machinery by inhibiting the master regulators HSF1 and IRE1 α . However, residual cancer cells that survive KRAS inhibition directly restore IRE1 α through an ER stress-independent unconventional phosphorylation mechanism that reestablishes proteostasis and sustains acquired resistance to KRAS inhibition.

In contrast to what occurs in nonmalignant cells (53), oncogenic KRAS activation resolves, rather than induces, ER stress in transformed

cancer cells through oncogenic kinase-dependent phosphorylation of IRE1 α . We identified four phosphorylation sites in IRE1 α that are distinct from IRE1 α autophosphorylation sites. The phosphorylation of IRE1 α at these sites prevents IRE1 α binding with the SEL1L/HRD1 E3 ligase complex, thus impairing the ubiquitination-dependent degradation of IRE1 α and stabilizing the protein. These sites are convergence points for multiple resistance pathways and function as a central gatekeeper of the rewired proteostasis network in the KRAS-resistant tumors. Inactivation of these sites is sufficient to abolish the direct regulation of IRE1 α by oncogenic signaling and collapse the reestablished proteostasis to overcome resistance to KRASi.

Despite the approval of sotorasib and adagrasib for the treatment of *KRAS*^{G12C}-mutant NSCLC patients, resistance to these inhibitors is rapid and almost inevitable (15, 18–29). The heterogeneous resistance mechanisms in patients and dose-limiting toxicity associated with targeting multiple resistance pathways—such as RTKs, MAPK, and PI3K—remain a major barrier to progress. Our mechanistic study directly addressed these clinical challenges by revealing IRE1 α -mediated proteostasis reprogramming as a convergence point for multiple heterogeneous resistance mechanisms in response to KRAS-MAPK inhibition. ORIN1001 is a highly specific IRE1 α RNase inhibitor (83) that demonstrates safety and tolerability in phase I clinical trial (NCT03950570) despite the occurrence of some adverse effects (86, 89). ORIN1001 substantially enhanced the responses of *KRAS*-mutant lung or pancreatic cancer PDX models to sotorasib or trametinib. These data demonstrate that directly targeting IRE1 α is a more effective and well-tolerated therapeutic strategy for reversing KRASi or MEKi resistance.

Our study reveals the direct cross-talk between oncogenic signaling and the protein quality control machinery. This study elucidated a molecular mechanism that accounts for the proteostasis modulation observed in response to KRAS inhibition. The mechanisms of KRASi resistance are heterogeneous in patients. Additional studies will be required to examine what proportion of KRAS-driven cancers that develop resistance to KRASi use IRE1 α -mediated mechanisms of resistance.

Materials and methods

Cell culture and treatment

MIA-PaCa-2, SW1990, PaTu 8988T, 293T, H358, and BEAS-2B cells were obtained from the American Type Culture Collection (ATCC). Patient-derived PATC53 and PATC148 cells were a gift from Dr. Michael Kim at The University of Texas MD Anderson Cancer Center (90). *iKras* cells were derived from our previously generated, doxycycline (Dox)-inducible, *Kras*^{G12D}-driven PDAC mouse model (*tetO-LSL-Kras*^{G12D/p53^{fl/fl}/^{+/p48-Cre/ROSA26-LSL-rtTA-IRES-GFP}) (55). *LSL-Kras*^{G12D} cells were derived from *Kras*^{G12D} knock-in PDAC mouse model (*LSL-Kras*^{G12D/p53^{fl/fl}/⁺) as described previously (55). The cell lines used in this study are listed in table S1. BEAS-2B cells were maintained in BEBM Bronchial Epithelial Cell Growth Basal Medium (Lonza, CC-3171) with growth factors and supplements from BEGM Bronchial Epithelial SingleQuots Kit (Lonza, CC-4175). Insulin and hEGF were withdrawn from the medium 48 hours before sample collection. H358, *iKras*, *LSL-Kras*^{G12D}, and PATC148 cells were maintained in RPMI supplemented with 10% FBS serum (Gibco, 10437028) and 100 μ g/ml penicillin/streptomycin (Invitrogen, 15140163).}}

H358^R cells were generated by in vitro culture of H358 cells with increasing dose of sotorasib for 6 months until the cells acquired resistance to 30 nM sotorasib. Doxycycline (VWR, AAJ60579-22, 1 μ g/ml) was added to the *iKras* cell culture medium to maintain *KRAS*^{G12D} expression. 10% charcoal stripped FBS (VWR, 97065-304) was used to culture *iKras* cells for doxycycline-withdrawal experiments as previously described (55). *iKras*^R cells were generated by in vitro culture of parental *iKras* cells in the absence of Dox until the cells acquired resistance to *KRAS*^{G12D} inactivation. MIA-PaCa-2, SW1990, PaTu 8988T, 293T and PATC53 cells were maintained in DMEM supplemented with 10% FBS (Gibco, 10437028) and 100 μ g/ml penicillin and streptomycin (Invitrogen, 15140163). MIA-PaCa-2^R cells were generated by in vitro culture of parental MIA-PaCa-2 cells with 30 nM sotorasib until the cells acquired resistance to KRAS inhibition. The chemicals used in this study are listed in table S2.

Tumor inoculation and treatment

The inoculation and establishment of PDX or xenograft tumors was described previously (90). PDAC19 and PDAC35 PDX models were generated by Baylor College of Medicine PDAC PDX Core. TC303AR PDX was generated by MD Anderson Cancer Center PDX Core. J000096652, TM00186, J00093018, and TM00192 PDX models were purchased from Jackson Laboratory. For tumor fragments transplantation of PDX, 1mm³ fresh tumor fragments were transplanted into the lower flanks of 6-week-old immune-compromised SCID/Beige mice (Charles river, strain code 250, CB17.Cg-*Prkdc*^{scid}*Lyst*^{bg/bg}/Crl, both female and male) or NRG mice (Jackson Laboratory, strain code 005557, NOD.Cg-*Prkdc*^{scid}*Il2rg*^{tm1Wjl}/SzJ, both female and male). For subcutaneous xenograft experiments, 1 × 10⁶ PATC53, SW1990, MIA-PaCa-2, H358 or *iKras* cells suspended in 100 μ l 50% Matrigel (Corning, #354230, in PBS) were injected subcutaneously into the lower flanks of 6-week-old SCID/Beige mice or Athymic Nude mice (Envigo, strain code 69, Hsd:Athymic Nude-*Foxn1*^{nu}, female). Tumor growth was monitored using calipers and tumor volumes were calculated by the equation $V(\text{mm}^3) = L \times W^2 / 2$, where L is the largest diameter and W is the perpendicular diameter. When tumors reached a volume of approximately 50–500 mm³, mice were randomized and treated with drugs as indicated. ORIN1001 was provided by Orinovo and suspended in 1% microcrystalline cellulose in 50% sucrose and sonicated for 90 min in water bath sonicator (VWR Ultrasonic Cleaner, Model 97043-964) before dosing at 150 mg/kg or 300 mg/kg body weight via daily oral gavage (83). Trametinib (1mg/kg) or sotorasib (30, 50, or 100 mg/kg) was formulated in the hydroxypropylmethylcellulose (HPMC)-Tween 80 buffer solution

(0.5% HPMC and 0.2% Tween 80, pH 8.0) and administered via daily oral gavage as described previously (12). SCH772984 (50mg/kg) was formulated in 45% saline, 50% PEG 400 and 5% DMSO, and administered via daily intraperitoneal injection. MK2206 (120 mg/kg) was formulated in 30% Captisol (Cydex) and administered by oral gavage every other day. All mice were maintained in accordance with Baylor College of Medicine Animal Care and Use Committee procedures and guidelines.

Protein aggregation detection assay

The PROTEOSTAT Aggresome detection kit (Enzo Life Sciences, ENZ-51035-K100), Congo red dye (CR, Sigma, 234610) or thioflavin T dye (ThT, Sigma, T3516) was used to detect misfolded or aggregated proteins in cells or tumor tissues (56, 72). The PROTEOSTAT aggresome detection assay was performed according to the manufacturer's instructions. Briefly, the *iKras* cells seeded on glass slides were washed with PBS, fixed with 4% formaldehyde for 30 min at room temperature (RT), permeabilized with Permeabilizing Solution (0.5% Triton X-100, 3mM EDTA) for 30 min on ice with gentle shake, and stained with the PROTEOSTAT dye (1:20,000 dilution) for 30 min at RT. MIA-PaCa-2 or H358 cells were trypsinized from culture dishes followed by washing, fixation, permeabilization and staining as described above. Tumor sections were deparaffinized and rehydrated before staining. Samples were incubated with PROTEOSTAT dye (1:20,000 dilution) for 30 min at RT. Nuclei were counterstained with DAPI. Cells treated with 10 μ M MG132 (provided in the PROTEOSTAT Aggresome detection kit) for 16 hours was used as positive control. Samples stained with DAPI only were used as negative control. Congo red (CR) and thioflavin T (ThT) staining were performed as described previously (56). Briefly, the *iKras* cells seeded on glass slides were washed with PBS, fixed with 4% formaldehyde for 30 min at RT, permeabilized with Permeabilizing Solution (0.5% Triton X-100, 3mM EDTA) for 30 min on ice with gentle shake, and stained with 20 μ M ThT or 50 nM CR dissolved in PBS for 30min at RT, followed by rinsing in PBS for 3 times. Nuclei were stained with DAPI.

Images (16-bit greyscale TIFFs) were analyzed using CellProfiler v2.2 (Broad Institute) as described previously (72). Briefly, the DAPI channel images were first smoothed with a median filter and nuclei were identified with automatic thresholding and a fixed diameter. The cell nuclei that touch the border of the image were eliminated for quantification. The cell nuclei that touch each other were separated with a watershed algorithm. Then, cell boundaries were identified by watershed gradient based on the dye signal of PROTEOSTAT, ThT or CR, using nuclei as a seed. Metrics for PROTEOSTAT, ThT, or CR were extracted from the cells.

Cell viability assay

Two hundred cells were seeded in 96-well plate and treated with different inhibitors as indicated in the figures. Cell viability was measured daily with CCK-8 kit (APEXBIO, # K1018). Briefly, 10 µl CCK-8 solution was added to each well and incubated for 1 hour at 37°C. The absorbance at 450 nm was measured using BioTek Synergy HTX Multi-Mode microplate reader.

Colony formation assay

Two hundred cells were seeded in 12-well plate and cultured for 5 days. Cells were washed with PBS, fixed with methanol and stained with 0.5% crystal violet. The colony number was counted and quantified.

BrdU incorporation assay

For BrdU staining, cells in the logarithmic phase of proliferation were first labeled with BrdU at a final concentration of 10 µM for 30 min at 37°C, followed by intracellular staining using the BrdU staining kit according to the manufacturer's instructions (BD Biosciences, 559619). Flow cytometry data were collected using BD FACS Diva 8 on a BD LSR II or BD Fortessa analyzer. The acquired data were analyzed using the FlowJo 10 software.

Luciferase assay

For *iKras* cells, the HSF1 firefly luciferase reporter was constructed by cloning 4 copies of the heat shock element (HSE) followed by a minimal promoter sequence (5'-AGAGGGTA-TATAATGGAAAGCTGACTTCCAG-3') (Promega, E375A) (all primer sequences are listed in table S3) into the SacI and HindIII sites of the pGL3-basic luciferase reporter (Promega, E1751). The construct was verified by DNA sequencing. The *iKras*^P or *iKras*^R cells were seeded in 96-well plate at 800 cells/well and co-transfected with 100ng *firefly* luciferase reporter and 5ng *Renilla* luciferase plasmid (pRL-TK, Promega, E2241, used as internal control) using Lipofectamine 3000 (Thermo Fisher, L3000008). The transfected *iKras*^P cells cultured in the presence or absence of Dox for 48 hours or the transfected *iKras*^R cells cultured in the absence of Dox were heat shocked at 43°C for 1 hour and recovered overnight before measuring the luciferase activities using the Dual-luciferase Reporter Assay System (Promega, #E1910) according to the manufacturer's instructions. For MIA-PaCa-2 cells, the same sequence (Promega, E375A) was cloned into the XhoI and BamHI sites of the pRRL-Luciferase plasmid (Addgene, 120798). The construct was verified by DNA sequencing. The *firefly* or pLenti.PGKblast-Renilla_Luciferase (Addgene, 74444) plasmid was packaged into lenti-viruses and infected MIA-PaCa-2^P or MIA-PaCa-2^R cells. After selection with blasticidin (20 µg/ml), the cells were seeded in 96-well plate at 800 cells/well. The infected MIA-PaCa-

2^P cells cultured in the presence or absence of sotorasib for 48 hours were heat shocked at 43°C for 1 hour and recovered overnight before measuring the luciferase activities using the Dual-luciferase Reporter Assay System (Promega, #E1910) according to the manufacturer's instructions.

Proteasome activity assay

The Proteasome Activity Fluorometric Assay Kit (BioVision, K245) was used to detect proteasome activity according to the manufacturer's instructions. Briefly, 1x10⁶ *iKras* cells from different treatments were homogenized in a tight-fitting bounce homogenizer (Thomas Scientific, 1176F27) with 500µl 0.5% NP-40 in PBS. 10 µl Proteasome Substrate (AMC-peptide, provided in the kit) was added to 10 µl cell lysate from each treatment group or 10 µl positive control lysate (provided in the kit) and mixed. The reaction was performed at 37°C and protected from light. The kinetics of fluorescence at excitation/emission = 350/440 nm were measured every 30 min using BioTek Synergy HTX Multi-Mode Plate Reader. Cells treated with 10µM MG132 (provided in the detection kit) for 16 hours were used as negative control. The fluorescence signals were normalized against total protein abundance detected with BCA Protein Assay Kit (Thermo Fisher Scientific, 23225).

Plasmids, virus production, and infection

The plasmids used are listed in table S4. The pRK5-Flag-IRE1α or pCDH-Flag-IRE1α was generated by cloning the full-length human IRE1α into pRK5 (Genentech) or pCDH (System Biosciences, CD511B-1) vector. The point mutations of IRE1α were introduced with Q5 Site-Directed Mutagenesis Kit (New England Biolabs, E0554). All the IRE1α plasmids are shRNA-resistant and listed in table S4. Primers used for cloning are listed in table S3. pHAGE-BRAF^{V600E}, pHAGE-MEK^{DD}, and pHAGE-PIK3CA^{H1047R} plasmids were generated as described previously (91). The pCDH-HA-Myr-AKT plasmid was purchased from Addgene (# 46969) (92). pLVX-Flag-HA-HRD1 was generated as described previously (73). The shRNAs targeting mouse *Xbp1*, *Ire1a*, *Perk*, *Gcn2*, *Hri*, *Pkr*, and *Scp3* were cloned into pLKO.1-TRC (Addgene, 10878). The shRNAs targeting human *XBPI*, *IRE1a*, *NcK*, and *PERK* were cloned in pLKO.1-TRC (Addgene 10878) or pLKO-Tet-On (Addgene 21915) vector to generate constitutive or inducible constructs. The shRNA sequences are listed in table S3. The pLKO.1 shScramble (Addgene 1864) or pLKO.1 Tet-On shScramble (same shRNA sequence as in pLKO.1 shScramble) was used as control. The p-GIPZ non-silencing shRNA control, p-GIPZ-MAPK1, p-GIPZ-MAPK3 were from Dharmacon Reagents. The Cas9-expressing plasmid lentiCas9-Blast was purchased from Addgene (#52962) (93). The gRNAs

targeting *Ire1a* or *Xbp1* were cloned into lentiGuide-Puro vector (Addgene, #52963). All gRNA sequences are listed in table S3. Plasmids containing coding sequence of different phosphatases are listed in table S4. To generate lentiviruses, 293T cells were co-transfected with psPAX2 and pMD2.G using Lipofectamine 3000 (Thermo Fisher Scientific, # L3000008). Lentiviruses were collected 48 and 72 hours after transfection and used for infecting cells in the presence of 8 µg/ml polybrene (Millipore Sigma, TR-1003-G) prior to puromycin selection (2 µg/ml, Millipore Sigma, P8833).

Generation of knock-out (KO) cells

To generate *Ire1a* or *Xbp1* KO cells, *iKras* cells were first infected with lentiviruses encoding Cas9 (lentiCas9-Blast, Addgene 52962) (93) and selected with 10 µg/ml blasticidin (Santa Cruz, 3513-03-09). The Cas9-expressing cells were then infected with lentiviruses expressing two gRNAs targeting the same exon and selected with puromycin (2µg/ml, Millipore-Sigma, P8833) to generate pooled KO cells. The gRNA sequences are listed in table S3.

Immunohistochemical (IHC) staining

Tumor specimens were fixed with freshly made 4% paraformaldehyde for 24 hours, washed with PBS and stored in 70% ethanol until paraffin embedding. IHC staining was performed on 5 µm-thick paraffin sections. For p-ERK, p-HSF1, p-GCN2, p-eIF2α, and YAP1 staining, 10mM sodium citrate buffer (pH 6.0) was used for antigen retrieval. For IRE1α, p-PERK, ATF4 and p-AKT IHC, 1mM EDTA buffer (pH 9.0) was used for antigen retrieval. Endogenous peroxidase was quenched with 3% H₂O₂ for 20 min followed by blocking with 3% normal goat serum. The following primary antibodies were used: IRE1α (1:20, Cell Signaling Technology, 3294); p-ERK (1:200, Cell Signaling Technology, 4376); and p-HSF1 (1:200, Life Technologies, BSM-52166R); p-PERK (1:25, Cell Signaling Technology, 3179); ATF4 (1:50, Santa Cruz, 390063); p-GCN2 (1:200, Thermo Fisher, PA5-105886); p-AKT (1:50, Cell Signaling Technology, 4060); p-eIF2α(1:50, Cell Signaling Technology, 9721); YAP1 (1:400, Cell Signaling Technology, 14074). Slides were incubated with ImmPRESS Excel HRP Goat Anti-Rabbit Polymer Reagent (Vector labs, MP-7451-15) for 30 min. Sections were developed with DAB+ solution (Dako, K3468) and counterstained with Harris Hematoxylin. The antibody used are listed in table S5.

Tissue microarray (TMA) analysis

For quantifications of TMA staining, TMAs stained with anti-IRE1α or anti-p-ERK antibody were scanned using the Aperio scanner and analyzed with QuPath software (94). Detailed tutorials of the software can be found at <https://qupath.readthedocs.io/en/stable/index.html>.

Briefly, images were preprocessed by automated “TMA dearraying” and “stain” vector estimation. Tissue sections were identified by running “simple tissue detection.” The “positive cell detection” command was used to detect DAB staining intensity. The score compartment was set as “DAB OD mean.” Tumor cells and stromal cells were classified by “training object classifier” based on annotations. The fraction score was calculated as the proportion of positively stained tumor cells (0%-100%). The intensity and fraction scores were then multiplied to obtain the H-score.

RNA extraction and real-time quantitative reverse-transcriptase PCR

Total RNA was extracted using TRIzol (Thermo Fisher Scientific, 15596026). Total RNA (1 µg) was converted to cDNA using the High-Capacity cDNA Reverse Transcription Kit (Applied Biosystems, 4368813), followed by qPCR on a QuantStudio 6 Flex Real-Time PCR System (Applied Biosystems). The sequences of all primers are listed in table S3.

Detergent-insoluble aggregates detection

Detergent-insoluble aggregates detection was performed as described previously (47). Briefly, cells with different treatments were harvested by trypsinization. After washing with cold PBS, 1×10^6 cells were lysed with RIPA buffer (25 mM Tris-HCl pH7.6, 150 mM NaCl, 1% Triton X-100, 1% sodium deoxycholate, 0.1% SDS, 1.5 mM EDTA) supplemented with protease inhibitor cocktail (Roche, 14826500), phosphatase inhibitor cocktail (Sigma, 4906845001) and 10 mM N-Ethylmaleimide (Sigma, E3876). Protein lysates were cleared by centrifugation at 16,000 g for 20 min at 4°C. The remaining insoluble pellets were then washed with RIPA buffer for three times to remove any remaining detergent-soluble proteins. The pellet containing detergent-insoluble aggregates was solubilized with urea buffer (8 M urea, 2% SDS, 50 mM DTT, 50 mM Tris-HCl pH7.4) for Western blot analysis. 3×10^5 cells were directly lysed in urea buffer (8 M urea, 2% SDS, 50 mM DTT, 50 mM Tris-HCl pH7.4) serving as loading control.

Coimmunoprecipitation

The co-immunoprecipitation (co-IP) assay was performed as previously described (73). Briefly, 293T cells transfected with different plasmids or H358 cells infected with indicated viruses were lysed with lysis buffer (50 mM Tris-HCl pH7.5, 150 mM NaCl, 1 mM EDTA, 1% Triton X-100) supplemented with protease inhibitor cocktail (Roche, 14826500) and phosphatase inhibitor cocktail (Sigma, 4906845001). Protein lysates were cleared by centrifugation at 12,000 g for 20 min at 4°C. Supernatant was incubated with anti-Flag M2 beads (Sigma, F-2426) or anti-Myc beads (Sigma, E-6654) for 4 h to overnight at 4°C with gentle rotating.

The beads were then washed once with lysis buffer, followed by additional three washes with wash buffer (50 mM Tris-HCl pH7.5, 150 mM NaCl, 1 mM EDTA, 1% Triton X-100, 10% glycerol). The proteins were eluted by boiling in 2 × Laemmli sample buffer [65.8 mM Tris-HCl, pH 6.8, 2.1% SDS, 26.3% (w/v) glycerol, 355 mM β-mercaptoethanol, 0.01% bromophenol blue] and analyzed by SDS-PAGE and Western blot.

Ubiquitination and phosphorylation assay

The ubiquitination and phosphorylation assays were performed to detect IRE1α ubiquitination and phosphorylation. MIA-PaCa-2 or H358 cells infected with lentiviruses encoding control or Flag-IRE1α were treated with DMSO, sotorasib or trametinib as described in figure legend and lysed with RIPA buffer (25 mM Tris-HCl pH7.6, 150 mM NaCl, 1% Triton X-100, 1% sodium deoxycholate, 0.1% SDS, 1.5 mM EDTA) supplemented with protease inhibitor cocktail (Roche, 14826500), phosphatase inhibitor cocktail (Sigma, 4906845001) and 10 mM N-Ethylmaleimide (Sigma, E3876). Protein lysates were sonicated for 30 s and cleared by centrifugation at 12,000 g for 20 min at 4°C. Supernatant was incubated with anti-Flag M2 beads (Sigma, F-2426) for 4 h at 4°C with gentle rotating. The beads were then washed with RIPA buffer for three times. The immunoprecipitates were eluted and denatured by boiling for 10 min in denature buffer (50 mM Tris-HCl pH7.6, 1% SDS, 0.5 mM EDTA, 1 mM DTT) to disrupt the interactions between immunoprecipitated IRE1α and its interacting proteins. The denatured elutes were diluted 1:10 with lysis buffer (50 mM Tris-HCl pH7.6, 150 mM NaCl, 1 mM EDTA, 1% Triton X-100) and subjected to a second-round immunoprecipitation with anti-Flag M2 beads (Sigma, F-2426) (4 h at 4°C) to remove all the interacting proteins and selectively pull down only IRE1α protein which allows for the specific analysis IRE1α ubiquitination and phosphorylation. The beads were then washed with RIPA buffer for three times. The proteins were eluted by boiling in 2 × Laemmli sample buffer [65.8 mM Tris-HCl pH 6.8, 2.1% SDS, 26.3% (w/v) glycerol, 355 mM β-mercaptoethanol, 0.01% bromophenol blue] and analyzed by SDS-PAGE and Western blot.

GST pull-down assay

The GST pull-down assay was performed to detect interaction between ERK and IRE1α. Briefly, recombinant GST or GST-ERK2 protein purified from *E.coli* (SignalChem, M28-10G-20) was incubated with recombinant His-IRE1α protein purified from Sf9 cells (83) in RIPA buffer (25 mM Tris-HCl pH7.6, 150 mM NaCl, 1% Triton X-100, 1% sodium deoxycholate, 0.1% SDS, 1.5 mM EDTA) for 30 min before the GSH-Sepharose beads (GE Healthcare, I7075601) were added and rotation for 1 hour at 4°C. The

beads were washed with RIPA buffer for three times. The proteins were eluted by boiling in 2 × Laemmli sample buffer and analyzed by SDS-PAGE and Western blot.

Flag pull-down assay

293T cells transfected with plasmid expressing Flag-GFP or Flag-IRE1α were lysed in RIPA buffer (25 mM Tris-HCl pH7.6, 150 mM NaCl, 1% Triton X-100, 1% sodium deoxycholate, 0.1% SDS, 1.5 mM EDTA, supplemented with protease inhibitor cocktail and phosphatase inhibitor cocktail) 48 hours after transfection. Protein lysates were cleared by centrifugation at 12,000 g for 20 min at 4°C. Supernatant was incubated with anti-Flag M2 beads (Sigma, F-2426) overnight at 4°C with gentle rotating. The beads were then washed with RIPA buffer for three times. These preloaded Flag M2 beads with Flag-GFP or Flag-IRE1α were then incubated with purified GST-ERK2 (SignalChem, M28-10G-20) for 30 min before washing with wash buffer (50 mM Tris-HCl pH7.5, 150 mM NaCl, 1 mM EDTA, 1% Triton X-100) for three times and elution by boiling in 2 × Laemmli sample buffer for 10 min. The eluents were analyzed by SDS-PAGE and Western blot.

In vitro kinase assay

Flag-GFP or Flag-IRE1α proteins were purified from 293T cells as described above. The Flag M2 beads pre-loaded with Flag-GFP or Flag-IRE1α proteins were rinsed with kinase assay buffer I (SignalChem, K01-09, 25 mM MOPS pH7.2, 12.5 mM β-glycerol-phosphate, 25 mM MgCl₂, 5 mM EGTA, 2 mM EDTA, 0.25 mM DTT) and subjected to in vitro kinase assay in the kinase assay buffer I plus 0.4 mM cold ATP and 1.0 µg GST-ERK2 activated by MEK1 in vitro (SignalChem, M28-10G-20). The reaction was carried out at 30°C for 30 min. The beads were then washed for three times with RIPA buffer (25 mM Tris-HCl pH7.6, 150 mM NaCl, 1% Triton X-100, 1% sodium deoxycholate, 0.1% SDS, 1.5 mM EDTA). The proteins were eluted by boiling in 2 × Laemmli sample buffer and analyzed by SDS-PAGE and Western blot.

For in vitro kinase assay labeled with [γ -³²P] ATP, Flag-IRE1α^{K599A} (kinase-dead form) or different mutated Flag-IRE1α^{K599A} proteins expressed in 293T cells were bound to anti-Flag M2 beads as described above and incubated with 0.5 µg GST-ERK2 activated by MEK1 in vitro (SignalChem, M28-10G-20) in the presence of 1 µCi of [γ -³²P] ATP (PerkinElmer, NEG002A100UC) and 0.4 mM cold ATP in the kinase buffer I (SignalChem, K01-09) for 30 min at 30°C. The reaction was stopped by boiling in 2 × Laemmli sample buffer for 10 min. The eluted proteins were resolved by SDS-PAGE and detected by autoradiography.

For in vitro kinase assay with recombinant His-IRE1α, 1.0 µg protein purified from Sf9 cells (83) and recombinant GST-ERK2 protein,

the reaction was carried out in the kinase assay buffer I (SignalChem, K01-09) plus 0.4 mM cold ATP for 30 min at 30°C. The reaction was stopped by adding 8 M urea buffer followed by purification of His-IRE1α with Ni-NTA agarose (QIAGEN, 30210). The proteins were eluted with 2 × Laemmli sample buffer by boiling for 10 min and analyzed by SDS-PAGE and Western blot.

In vitro phosphatase assay

The in vitro phosphatase assay was performed as described previously (95). Phosphorylated Flag-IRE1α proteins were purified from 293T cells expressing MEK^{DD} as described above. The Flag M2 beads pre-loaded with phosphorylated Flag-IRE1α proteins were rinsed with phosphatase assay buffer (40 mM Tris-HCl pH7.5, 20 mM KCl, 10 mM MnCl₂, and 2 mM DTT) and subjected to in vitro phosphatase assay in the phosphatase assay buffer and 1.0 µg recombinant His-SCP3 protein (NOVUS, NBPI-99109). The reaction was carried out at 30°C for 30 min. The beads were then washed for three times with RIPA buffer (25 mM Tris-HCl pH7.6, 150 mM NaCl, 1% Triton X-100, 1% sodium deoxycholate, 0.1% SDS, 1.5 mM EDTA). The proteins were eluted by boiling in 2 × Laemmli sample buffer and analyzed by SDS-PAGE. UV transmission (GE Healthcare Lifer Sciences) was used to detect ORIN1001 that is covalently bound to IRE1α protein in the SDS-PAGE.

Biochemical fluorescence assay to detect IRE1α interaction with ORIN1001

The in vitro binding assay to detect IRE1α with ORIN1001 was performed as described previously (96). Briefly, WT or V918F mutant Flag-IRE1α proteins were purified from 293T cells as described above. The Flag M2 beads pre-loaded with equal amount of Flag-IRE1α^{WT} or Flag-IRE1α^{V918F} proteins were incubated with 200 µM ORIN1001 in binding buffer (50 mM Tris-HCl pH7.5, 100 mM NaCl, 10% Glycerol, 1% Triton X-100, 50 mM EDTA) for 3 hours at 4°C. After that, 6 mM NaBH₄ was added to reduce the imine (Schiff base) between IRE1α and ORIN1001 to stable amine. The beads were then extensively washed for three times with binding buffer and three times with RIPA buffer (25 mM Tris-HCl pH7.6, 150 mM NaCl, 1% Triton X-100, 1% sodium deoxycholate, 0.1% SDS, 1.5 mM EDTA). The proteins were eluted by boiling in 2 × Laemmli sample buffer and analyzed by SDS-PAGE. UV transmission (GE Healthcare Lifer Sciences) was used to detect ORIN1001 that is covalently bound to IRE1α protein in the SDS-PAGE.

Modelling of the IRE1α-ORIN1001 complex

Murine IRE1α and MKC9989 (PDB 4PL3) was used as a template to model ORIN1001 bound to murine IRE1α with Schrodinger software. Homology modelling of yeast IRE1α (PDB 3FBV) was also achieved and was superimposed manually onto the model of ORIN1001 with murine IRE1α.

Clinical Proteomic Tumor Analysis Consortium (CPTAC) data analysis

Correlation between IRE1α phosphorylation (S549) and ERK phosphorylation (Y204) in CPTAC NSCLC tumors were analyzed using the LinkedOmics platform (97) (<http://www.linkedomics.org>).

Western blot

Whole cell lysates or immunoprecipitation samples were separated by SDS-PAGE and transferred to nitrocellulose membrane (Bio-rad, 1620112). The antibody used are listed in table S5. The reagents and kits used in this study are listed in table S2.

Statistics and reproducibility

Data are expressed as the mean ± SD or mean ± SEM as indicated in the figure legends; *n* is the number of independent biological replicates, unless specifically indicated otherwise in the figure legend. The respective *n* values are shown in the figure legends. No statistical method was used to pre-determine the sample sizes. For animal experiments, at least 4 biological replicates were included based on previously published work, preliminary studies as standard for this field of research. See figures legends for each experiment. Treatments were

performed in a non-blinded manner by a research technician who was not aware of the objectives of the study because the colors of the drugs used are different from that of vehicle control. The results were quantified using GraphPad Prism 8. Two-tailed, unpaired Student's *t* test with or without Welch's correction was utilized to compare the differences between 2 groups as indicated in figure legends. One-way ANOVA with Dunnett's or Tukey's multiple comparison test was used to compare the differences among 3 or more groups as indicated in figure legends. Two-way ANOVA with Bonferroni's multiple comparison test was used to calculate the significance difference for cell growth, tumor volume and body weight measurement over time. The log-rank (Mantel-Cox) test was used to test for the significant differences of survival between the groups. *P* < 0.05 was considered statistically significant. No samples or animals were excluded from the analysis.

Study approval

All protocols described in this study were approved by the Baylor College of Medicine Institutional Animal Care and Use Committee (AN6813).

REFERENCES AND NOTES

- A. J. Scheidig, C. Burmester, R. S. Goody, The pre-hydrolysis state of p21(“)⁰ in complex with GTP: New insights into the role of water molecules in the GTP hydrolysis reaction of ras-like proteins. *Structure* **7**, 1311–1324 (1999). doi: [10.1016/S0969-2126\(00\)80021-0](https://doi.org/10.1016/S0969-2126(00)80021-0); pmid: 10574788
- K. Scheffzek *et al.*, The Ras-RasGAP complex: Structural basis for GTPase activation and its loss in oncogenic Ras mutants. *Science* **277**, 333–338 (1997). doi: [10.1126/science.277.5324.333](https://doi.org/10.1126/science.277.5324.333); pmid: 9219684
- G. Bollag, F. McCormick, Differential regulation of rasGAP and neurofibromatosis gene product activities. *Nature* **351**, 576–579 (1991). doi: [10.1038/351576a0](https://doi.org/10.1038/351576a0); pmid: 1904555
- C. Li *et al.*, The G protein signaling regulator RGS3 enhances the GTPase activity of KRAS. *Science* **374**, 197–201 (2021). doi: [10.1126/science.abf1730](https://doi.org/10.1126/science.abf1730); pmid: 34618566
- J. P. McGrath, D. J. Capon, D. V. Goedel, A. D. Levinson, Comparative biochemical properties of normal and activated human ras p21 protein. *Nature* **310**, 644–649 (1984). doi: [10.1038/310644a0](https://doi.org/10.1038/310644a0); pmid: 6147754
- J. Downward, Targeting RAS signalling pathways in cancer therapy. *Nat. Rev. Cancer* **3**, 11–22 (2003). doi: [10.1038/nrc969](https://doi.org/10.1038/nrc969); pmid: 12509763
- D. K. Simanshu, D. V. Nissley, F. McCormick, RAS proteins and their regulators in human disease. *Cell* **170**, 17–33 (2017). doi: [10.1016/j.cell.2017.06.009](https://doi.org/10.1016/j.cell.2017.06.009); pmid: 28666118
- A. D. Cox, S. W. Fesik, A. C. Kimmelman, J. Luo, C. J. Der, Drugging the undruggable RAS: Mission possible? *Nat. Rev. Drug Discov.* **13**, 828–851 (2014). doi: [10.1038/nrd4389](https://doi.org/10.1038/nrd4389); pmid: 25323927
- J. Encarnación-Rosado, A. C. Kimmelman, Harnessing metabolic dependencies in pancreatic cancers. *Nat. Rev. Gastroenterol. Hepatol.* **18**, 482–492 (2021). doi: [10.1038/s41575-021-00431-7](https://doi.org/10.1038/s41575-021-00431-7); pmid: 33742165
- Y. Pylayeva-Gupta, E. Grabocka, D. Bar-Sagi, RAS oncogenes: Weaving a tumorigenic web. *Nat. Rev. Cancer* **11**, 761–774 (2011). doi: [10.1038/nrc3106](https://doi.org/10.1038/nrc3106); pmid: 21993244
- J. M. Ostrem, U. Peters, M. L. Sos, J. A. Wells, K. M. Shokat, K-Ras(G12C) inhibitors allosterically control GTP affinity and effector interactions. *Nature* **503**, 548–551 (2013). doi: [10.1038/nature12796](https://doi.org/10.1038/nature12796); pmid: 24256730
- J. Canor *et al.*, The clinical KRAS(G12C) inhibitor AMG 510 drives anti-tumour immunity. *Nature* **575**, 217–223 (2019). doi: [10.1038/s41586-019-1694-1](https://doi.org/10.1038/s41586-019-1694-1); pmid: 31666701
- J. Hallin *et al.*, The KRAS^{G12C} inhibitor MRTX849 provides insight toward therapeutic susceptibility of KRAS-mutant cancers in mouse models and patients. *Cancer Discov.* **10**,

- 54–71 (2020). doi: [10.1158/2159-8290.CD-19-1167](https://doi.org/10.1158/2159-8290.CD-19-1167); pmid: [31658955](https://pubmed.ncbi.nlm.nih.gov/31658955/)
14. F. Skoulidis et al., Sotorasib for lung cancers with KRAS p.G12C mutation. *N. Engl. J. Med.* **384**, 2371–2381 (2021). doi: [10.1056/NEJMoa2103695](https://doi.org/10.1056/NEJMoa2103695); pmid: [34096690](https://pubmed.ncbi.nlm.nih.gov/34096690/)
 15. D. S. Hong et al., KRAS^{G12C} inhibition with sotorasib in advanced solid tumors. *N. Engl. J. Med.* **383**, 1207–1217 (2020). doi: [10.1056/NEJMoa1917239](https://doi.org/10.1056/NEJMoa1917239); pmid: [32955176](https://pubmed.ncbi.nlm.nih.gov/32955176/)
 16. P. A. Jänne et al., Adagrasib in non-small-cell lung cancer harboring a KRAS^{G12C} mutation. *N. Engl. J. Med.* **387**, 120–131 (2022). doi: [10.1056/NEJMoa2204619](https://doi.org/10.1056/NEJMoa2204619); pmid: [35658005](https://pubmed.ncbi.nlm.nih.gov/35658005/)
 17. N. S. Akhave, A. B. Biter, D. S. Hong, Mechanisms of resistance to KRAS^{G12C}-targeted therapy. *Cancer Discov.* **11**, 1345–1352 (2021). doi: [10.1158/2159-8290.CD-20-1616](https://doi.org/10.1158/2159-8290.CD-20-1616); pmid: [33820777](https://pubmed.ncbi.nlm.nih.gov/33820777/)
 18. N. Tanaka et al., Clinical acquired resistance to KRASG12C inhibition through a novel KRAS switch-II pocket mutation and polyclonal alterations converging on RAS-MAPK reactivation. *Cancer Discov.* **11**, 1913–1922 (2021). doi: [10.1158/2159-8290.CD-21-0365](https://doi.org/10.1158/2159-8290.CD-21-0365); pmid: [33824136](https://pubmed.ncbi.nlm.nih.gov/33824136/)
 19. M. M. Awad et al., Acquired resistance to KRAS^{G12C} inhibition in cancer. *N. Engl. J. Med.* **384**, 2382–2393 (2021). doi: [10.1056/NEJMoa2105281](https://doi.org/10.1056/NEJMoa2105281); pmid: [34161704](https://pubmed.ncbi.nlm.nih.gov/34161704/)
 20. B. T. Li et al., Largest evaluation of acquired resistance to sotorasib in KRAS-p.G12C-mutated non-small cell lung cancer (NSCLC) and colorectal cancer (CRC): Plasma biomarker analysis of CodeBreak100. *J. Clin. Oncol.* **40**, 106–102 (2022). doi: [10.1200/JCO.2022.40.16_suppl.102](https://doi.org/10.1200/JCO.2022.40.16_suppl.102)
 21. Y. Zhao et al., Diverse alterations associated with resistance to KRAS(G12C) inhibition. *Nature* **599**, 679–683 (2021). doi: [10.1038/s41586-021-04065-2](https://doi.org/10.1038/s41586-021-04065-2); pmid: [34759319](https://pubmed.ncbi.nlm.nih.gov/34759319/)
 22. R. Yaeger et al., Molecular characterization of acquired resistance to KRASG12C-EGFR inhibition in colorectal cancer. *Cancer Discov.* **13**, 41–55 (2023). doi: [10.1158/2159-8290.CD-22-0405](https://doi.org/10.1158/2159-8290.CD-22-0405); pmid: [36355783](https://pubmed.ncbi.nlm.nih.gov/36355783/)
 23. Y. S. Tsai et al., Rapid idiosyncratic mechanisms of clinical resistance to KRAS G12C inhibition. *J. Clin. Invest.* **132**, e155523 (2022). doi: [10.1172/JCI155523](https://doi.org/10.1172/JCI155523); pmid: [34990404](https://pubmed.ncbi.nlm.nih.gov/34990404/)
 24. V. Amiodio et al., EGFR blockade reverts resistance to KRAS G12C inhibition in colorectal cancer. *Cancer Discov.* **10**, 1129–1139 (2020). doi: [10.1158/2159-8290.CD-20-0187](https://doi.org/10.1158/2159-8290.CD-20-0187); pmid: [32430388](https://pubmed.ncbi.nlm.nih.gov/32430388/)
 25. J. Y. Xue et al., Rapid non-uniform adaptation to conformation-specific KRAS(G12C) inhibition. *Nature* **577**, 421–425 (2020). doi: [10.1038/s41586-019-1884-x](https://doi.org/10.1038/s41586-019-1884-x); pmid: [31915379](https://pubmed.ncbi.nlm.nih.gov/31915379/)
 26. M. B. Ryan et al., Vertical pathway inhibition overcomes adaptive feedback resistance to KRAS^{G12C} inhibition. *Clin. Cancer Res.* **26**, 1633–1643 (2020). doi: [10.1158/1078-0432.CCR-19-3523](https://doi.org/10.1158/1078-0432.CCR-19-3523); pmid: [31776128](https://pubmed.ncbi.nlm.nih.gov/31776128/)
 27. W. S. Brown et al., Overcoming adaptive resistance to KRAS and MEK inhibitors by co-targeting mTORC1/2 complexes in pancreatic cancer. *Cell Rep. Med.* **1**, 100131 (2020). doi: [10.1016/j.xcrm.2020.100131](https://doi.org/10.1016/j.xcrm.2020.100131); pmid: [33294856](https://pubmed.ncbi.nlm.nih.gov/33294856/)
 28. M. Molina-Arcas et al., Development of combination therapies to maximize the impact of KRAS-G12C inhibitors in lung cancer. *Sci. Transl. Med.* **11**, eaaw7999 (2019). doi: [10.1126/scitranslmed.aaw7999](https://doi.org/10.1126/scitranslmed.aaw7999); pmid: [31534020](https://pubmed.ncbi.nlm.nih.gov/31534020/)
 29. S. Suzuki et al., KRAS inhibitor resistance in MET-amplified KRAS^{G12C} non-small cell lung cancer induced by RAS- and non-RAS-mediated cell signaling mechanisms. *Clin. Cancer Res.* **27**, 5697–5707 (2021). doi: [10.1158/1078-0432.CCR-21-0856](https://doi.org/10.1158/1078-0432.CCR-21-0856); pmid: [34365406](https://pubmed.ncbi.nlm.nih.gov/34365406/)
 30. S. R. Punekar, V. Velcheti, B. G. Neel, K. K. Wong, The current state of the art and future trends in RAS-targeted cancer therapies. *Nat. Rev. Clin. Oncol.* **19**, 637–655 (2022). doi: [10.1038/s41571-022-00671-9](https://doi.org/10.1038/s41571-022-00671-9); pmid: [36028717](https://pubmed.ncbi.nlm.nih.gov/36028717/)
 31. D. L. Longo, N. Rosen, Targeting oncogenic RAS protein. *N. Engl. J. Med.* **387**, 184–186 (2022). doi: [10.1056/NEJMoa2206831](https://doi.org/10.1056/NEJMoa2206831); pmid: [35830646](https://pubmed.ncbi.nlm.nih.gov/35830646/)
 32. V. Thatikonda et al., Combined KRAS^{G12C} and SOS1 inhibition enhances and extends the anti-tumor response in KRAS^{G12C}-driven cancers by addressing intrinsic and acquired resistance. *biorXiv* 252510 [Preprint] (2023); <https://doi.org/10.1101/2023.01.23.525210>.
 33. C. Fedele et al., SHP2 inhibition diminishes KRASG12C cycling and promotes tumor microenvironment remodeling. *J. Exp. Med.* **218**, e20201414 (2021). doi: [10.1084/jem.20201414](https://doi.org/10.1084/jem.20201414); pmid: [33045063](https://pubmed.ncbi.nlm.nih.gov/33045063/)
 34. C. S. L. Ho et al., HER2 mediates clinical resistance to the KRAS^{G12C} inhibitor sotorasib, which is overcome by co-targeting SHP2. *Eur. J. Cancer* **159**, 16–23 (2021). doi: [10.1016/j.ejca.2021.10.003](https://doi.org/10.1016/j.ejca.2021.10.003); pmid: [34715459](https://pubmed.ncbi.nlm.nih.gov/34715459/)
 35. M. B. Ryan et al., KRAS^{G12C}-independent feedback activation of wild-type RAS constrains KRAS^{G12C} inhibitor efficacy. *Cell Rep.* **39**, 110993 (2022). doi: [10.1016/j.celrep.2022.110993](https://doi.org/10.1016/j.celrep.2022.110993); pmid: [35732135](https://pubmed.ncbi.nlm.nih.gov/35732135/)
 36. M. Sattler, A. Mohanty, P. Kulkarni, R. Salgia, Precision oncology provides opportunities for targeting KRAS-inhibitor resistance. *Trends Cancer* **9**, 42–54 (2023). doi: [10.1016/j.trecan.2022.10.001](https://doi.org/10.1016/j.trecan.2022.10.001); pmid: [36751115](https://pubmed.ncbi.nlm.nih.gov/36751115/)
 37. A. Kapoor et al., Yap1 activation enables bypass of oncogenic Ras addiction in pancreatic cancer. *Cell* **158**, 185–197 (2014). doi: [10.1016/j.cell.2014.06.003](https://doi.org/10.1016/j.cell.2014.06.003); pmid: [24954535](https://pubmed.ncbi.nlm.nih.gov/24954535/)
 38. D. D. Shao et al., KRAS and YAP1 converge to regulate EMT and tumor survival. *Cell* **158**, 171–184 (2014). doi: [10.1016/j.cell.2014.06.004](https://doi.org/10.1016/j.cell.2014.06.004); pmid: [24954536](https://pubmed.ncbi.nlm.nih.gov/24954536/)
 39. G. H. Fisher et al., Induction and apoptotic regression of lung adenocarcinomas by regulation of a K-Ras transgene in the presence and absence of tumor suppressor genes. *Genes Dev.* **15**, 3249–3262 (2001). doi: [10.1101/gad.947701](https://doi.org/10.1101/gad.947701); pmid: [11751631](https://pubmed.ncbi.nlm.nih.gov/11751631/)
 40. S. Joshi et al., Adapting to stress—Chaperome networks in cancer. *Nat. Rev. Cancer* **18**, 562–575 (2018). doi: [10.1038/s41568-018-0020-9](https://doi.org/10.1038/s41568-018-0020-9); pmid: [29795326](https://pubmed.ncbi.nlm.nih.gov/29795326/)
 41. X. Chen, J. R. Cubillos-Ruiz, Endoplasmic reticulum stress signals in the tumour and its microenvironment. *Nat. Rev. Cancer* **21**, 71–88 (2021). doi: [10.1038/s41568-020-00312-2](https://doi.org/10.1038/s41568-020-00312-2); pmid: [33214692](https://pubmed.ncbi.nlm.nih.gov/33214692/)
 42. J. Labbadia, R. I. Morimoto, The biology of proteostasis in aging and disease. *Annu. Rev. Biochem.* **84**, 435–464 (2015). doi: [10.1146/annurev-biochem-060614-033955](https://doi.org/10.1146/annurev-biochem-060614-033955); pmid: [25784053](https://pubmed.ncbi.nlm.nih.gov/25784053/)
 43. P. Walter, D. Ron, The unfolded protein response: From stress pathway to homeostatic regulation. *Science* **334**, 1081–1086 (2011). doi: [10.1126/science.1209038](https://doi.org/10.1126/science.1209038); pmid: [22116877](https://pubmed.ncbi.nlm.nih.gov/22116877/)
 44. M. Wang, R. J. Kaufman, Protein misfolding in the endoplasmic reticulum as a conduit to human disease. *Nature* **529**, 326–335 (2016). doi: [10.1038/nature17041](https://doi.org/10.1038/nature17041); pmid: [26791723](https://pubmed.ncbi.nlm.nih.gov/26791723/)
 45. A. Almanza et al., Endoplasmic reticulum stress signalling – from basic mechanisms to clinical applications. *FEBS J.* **286**, 241–278 (2019). doi: [10.1111/febs.14608](https://doi.org/10.1111/febs.14608); pmid: [30027602](https://pubmed.ncbi.nlm.nih.gov/30027602/)
 46. R. Gomez-Pastor, E. T. Burchfield, D. J. Thiele, Regulation of heat shock transcription factors and their roles in physiology and disease. *Nat. Rev. Mol. Cell Biol.* **19**, 4–19 (2018). doi: [10.1038/nrm.2017.73](https://doi.org/10.1038/nrm.2017.73); pmid: [28852200](https://pubmed.ncbi.nlm.nih.gov/28852200/)
 47. Z. Tang et al., MEK guards proteome stability and inhibits tumor-suppressive amyloidogenesis via HSF1. *Cell* **160**, 729–744 (2015). doi: [10.1016/j.cell.2015.01.028](https://doi.org/10.1016/j.cell.2015.01.028); pmid: [25679764](https://pubmed.ncbi.nlm.nih.gov/25679764/)
 48. H. J. Clarke, J. E. Chambers, E. Liniker, S. J. Marciniak, Endoplasmic reticulum stress in malignancy. *Cancer Cell* **25**, 563–573 (2014). doi: [10.1016/j.ccr.2014.03.015](https://doi.org/10.1016/j.ccr.2014.03.015); pmid: [24823636](https://pubmed.ncbi.nlm.nih.gov/24823636/)
 49. J. S. Cox, C. E. Shamu, P. Walter, Transcriptional induction of genes encoding endoplasmic reticulum resident proteins requires a transmembrane protein kinase. *Cell* **73**, 1197–1206 (1993). doi: [10.1016/0092-8674\(93\)90648-A](https://doi.org/10.1016/0092-8674(93)90648-A); pmid: [8513503](https://pubmed.ncbi.nlm.nih.gov/8513503/)
 50. K. Mori, W. Ma, M.-J. Gethin, J. Sambrook, A transmembrane protein with a cdc2+CDC28-related kinase activity is required for signaling from the ER to the nucleus. *Cell* **74**, 743–756 (1993). doi: [10.1016/0092-8674\(93\)90521-Q](https://doi.org/10.1016/0092-8674(93)90521-Q); pmid: [8358794](https://pubmed.ncbi.nlm.nih.gov/8358794/)
 51. H. Yoshida, T. Matsui, A. Yamamoto, T. Okada, K. Mori, XBP1 mRNA is induced by ATF6 and spliced by IRE1 in response to ER stress to produce a highly active transcription factor. *Cell* **107**, 881–891 (2001). doi: [10.1016/S0092-8674\(01\)00611-0](https://doi.org/10.1016/S0092-8674(01)00611-0); pmid: [11779464](https://pubmed.ncbi.nlm.nih.gov/11779464/)
 52. M. Calfon et al., IRE1 couples endoplasmic reticulum load to secretory capacity by processing the XBP-1 mRNA. *Nature* **415**, 92–96 (2002). doi: [10.1038/415092a](https://doi.org/10.1038/415092a); pmid: [11780124](https://pubmed.ncbi.nlm.nih.gov/11780124/)
 53. C. Denoyelle et al., Anti-oncogenic role of the endoplasmic reticulum differentially affected by mutations in the MAPK pathway. *Nat. Cell Biol.* **8**, 1053–1063 (2006). doi: [10.1038/ncb1471](https://doi.org/10.1038/ncb1471); pmid: [16964246](https://pubmed.ncbi.nlm.nih.gov/16964246/)
 54. T. Šušić et al., A role for the unfolded protein response stress sensor ERNL1 in regulating the response to MEK inhibitors in KRAS mutant colon cancers. *Genome Med.* **10**, 90 (2018). doi: [10.1186/s13073-018-0600-z](https://doi.org/10.1186/s13073-018-0600-z); pmid: [30482246](https://pubmed.ncbi.nlm.nih.gov/30482246/)
 55. H. Ying et al., Oncogenic Ras maintains pancreatic tumors through regulation of anabolic glucose metabolism. *Cell* **149**, 656–670 (2012). doi: [10.1016/j.cell.2012.01.058](https://doi.org/10.1016/j.cell.2012.01.058); pmid: [22541435](https://pubmed.ncbi.nlm.nih.gov/22541435/)
 56. M. R. Nilsson, Techniques to study amyloid fibril formation in vitro. *Methods* **34**, 151–160 (2004). doi: [10.1016/j.jymeth.2004.03.012](https://doi.org/10.1016/j.jymeth.2004.03.012); pmid: [15283924](https://pubmed.ncbi.nlm.nih.gov/15283924/)
 57. M. Galves, R. Rath, G. Prag, A. Ashkenazi, Ubiquitin signaling and degradation of aggregate-prone proteins. *Trends Biochem. Sci.* **44**, 872–884 (2019). doi: [10.1016/j.tibs.2019.04.007](https://doi.org/10.1016/j.tibs.2019.04.007); pmid: [31079890](https://pubmed.ncbi.nlm.nih.gov/31079890/)
 58. C. L. Klaips, G. G. Jayaram, F. U. Hartl, Pathways of cellular proteostasis in aging and disease. *J. Cell Biol.* **217**, 51–63 (2018). doi: [10.1083/jcb.201709072](https://doi.org/10.1083/jcb.201709072); pmid: [29127110](https://pubmed.ncbi.nlm.nih.gov/29127110/)
 59. L. Cortez, V. Sim, The therapeutic potential of chemical chaperones in protein folding diseases. *Prion* **8**, 197–202 (2014). doi: [10.4161/pri.28938](https://doi.org/10.4161/pri.28938); pmid: [24818993](https://pubmed.ncbi.nlm.nih.gov/24818993/)
 60. F. Englin et al., Restoration of the unfolded protein response in pancreatic β cells protects mice against type 1 diabetes. *Sci. Transl. Med.* **5**, 21ra156 (2013). doi: [10.1126/scitranslmed.3006534](https://doi.org/10.1126/scitranslmed.3006534); pmid: [24225943](https://pubmed.ncbi.nlm.nih.gov/24225943/)
 61. M. Costa-Mattioli, P. Walter, The integrated stress response: From mechanism to disease. *Science* **368**, eaat5314 (2020). doi: [10.1126/science.aat5314](https://doi.org/10.1126/science.aat5314); pmid: [32327570](https://pubmed.ncbi.nlm.nih.gov/32327570/)
 62. T. Guettouche, F. Boellmann, W. S. Lane, R. Voellmy, Analysis of phosphorylation of human heat shock factor 1 in cells experiencing a stress. *BMC Biochem.* **6**, 4 (2005). doi: [10.1186/1471-2091-6-4](https://doi.org/10.1186/1471-2091-6-4); pmid: [15760475](https://pubmed.ncbi.nlm.nih.gov/15760475/)
 63. W. Tirasophon, A. A. Welihinda, R. J. Kaufman, A stress response pathway from the endoplasmic reticulum to the nucleus requires a novel bifunctional protein kinase/endoribonuclease (IRE1) in mammalian cells. *Genes Dev.* **12**, 1812–1824 (1998). doi: [10.1101/gad.12.12.1812](https://doi.org/10.1101/gad.12.12.1812); pmid: [9637683](https://pubmed.ncbi.nlm.nih.gov/9637683/)
 64. J. Hollien, J. S. Weissman, Decay of endoplasmic reticulum-localized mRNAs during the unfolded protein response. *Science* **313**, 104–107 (2006). doi: [10.1126/science.1129631](https://doi.org/10.1126/science.1129631); pmid: [16825573](https://pubmed.ncbi.nlm.nih.gov/16825573/)
 65. S. Lhomond et al., Dual IRE1 RNase functions dictate glioblastoma development. *EMBO Mol. Med.* **10**, e7929 (2018). doi: [10.15252/emmm.201707929](https://doi.org/10.15252/emmm.201707929); pmid: [29311133](https://pubmed.ncbi.nlm.nih.gov/29311133/)
 66. C. Fedele et al., SHP2 inhibition prevents adaptive resistance to MEK inhibitors in multiple cancer models. *Cancer Discov.* **8**, 1237–1249 (2018). doi: [10.1158/2159-8290.CD-18-0444](https://doi.org/10.1158/2159-8290.CD-18-0444); pmid: [30045908](https://pubmed.ncbi.nlm.nih.gov/30045908/)
 67. S. Mainardi et al., SHP2 is required for growth of KRAS-mutant non-small-cell lung cancer in vivo. *Nat. Med.* **24**, 961–967 (2018). doi: [10.1038/s41591-018-0023-9](https://doi.org/10.1038/s41591-018-0023-9); pmid: [29808006](https://pubmed.ncbi.nlm.nih.gov/29808006/)
 68. R. J. Nichols et al., RAS nucleotide cycling underlies the SHP2 phosphatase dependence of mutant BRAF, NF1- and RAS-driven cancers. *Nat. Cell Biol.* **20**, 1064–1073 (2018). doi: [10.1038/s41556-018-0169-1](https://doi.org/10.1038/s41556-018-0169-1); pmid: [30104724](https://pubmed.ncbi.nlm.nih.gov/30104724/)
 69. D. A. Ruess et al., Mutant KRAS-driven cancers depend on PTPN11/SHP2 phosphatase. *Nat. Med.* **24**, 954–960 (2018). doi: [10.1038/s41591-018-0024-8](https://doi.org/10.1038/s41591-018-0024-8); pmid: [29808009](https://pubmed.ncbi.nlm.nih.gov/29808009/)
 70. S. Sun et al., IRE1α is an endogenous substrate of endoplasmic-reticulum-associated degradation. *Nat. Cell Biol.* **17**, 1546–1555 (2015). doi: [10.1038/ncb3266](https://doi.org/10.1038/ncb3266); pmid: [26551274](https://pubmed.ncbi.nlm.nih.gov/26551274/)
 71. J. L. Brodsky, Cleaning up: ER-associated degradation to the rescue. *Cell* **151**, 1163–1167 (2012). doi: [10.1016/j.cell.2012.11.012](https://doi.org/10.1016/j.cell.2012.11.012); pmid: [23217703](https://pubmed.ncbi.nlm.nih.gov/23217703/)
 72. X. Liu et al., Notch-induced endoplasmic reticulum-associated degradation governs mouse thymocyte β-selection. *eLife* **10**, e69975 (2021). doi: [10.7554/elife.69975](https://doi.org/10.7554/elife.69975); pmid: [34240701](https://pubmed.ncbi.nlm.nih.gov/34240701/)
 73. L. Xu et al., Protein quality control through endoplasmic reticulum-associated degradation maintains haematopoietic stem cell identity and niche interactions. *Nat. Cell Biol.* **22**, 1162–1169 (2020). doi: [10.1038/s41556-020-00581-x](https://doi.org/10.1038/s41556-020-00581-x); pmid: [32958856](https://pubmed.ncbi.nlm.nih.gov/32958856/)
 74. H. Meyer, M. Bug, S. Bremer, Emerging functions of the VCP/p97 AAA-ATPase in the ubiquitin system. *Nat. Cell Biol.* **14**, 117–123 (2012). doi: [10.1038/ncb2407](https://doi.org/10.1038/ncb2407); pmid: [22998039](https://pubmed.ncbi.nlm.nih.gov/22998039/)
 75. D. J. Anderson et al., Targeting the AAA ATPase p97 as an approach to treat cancer through disruption of protein homeostasis. *Cancer Cell* **28**, 653–665 (2015). doi: [10.1016/j.ccr.2015.10.002](https://doi.org/10.1016/j.ccr.2015.10.002); pmid: [26555175](https://pubmed.ncbi.nlm.nih.gov/26555175/)
 76. R. Roskoski Jr., ERK1/2 MAP kinases: Structure, function, and regulation. *Pharmacol. Res.* **66**, 105–143 (2012). doi: [10.1016/j.phrs.2012.04.005](https://doi.org/10.1016/j.phrs.2012.04.005); pmid: [22695282](https://pubmed.ncbi.nlm.nih.gov/22695282/)
 77. S. Satpathy et al., A proteogenomic portrait of lung squamous cell carcinoma. *Cell* **184**, 4348–4371.e40 (2021). doi: [10.1016/j.cell.2021.07.016](https://doi.org/10.1016/j.cell.2021.07.016); pmid: [34358469](https://pubmed.ncbi.nlm.nih.gov/34358469/)
 78. K. You et al., QIRCH1 dictates the outcome of ER stress through transcriptional control of proteostasis. *Science* **371**, eabb6896 (2021). doi: [10.1126/science.abb6896](https://doi.org/10.1126/science.abb6896); pmid: [33384352](https://pubmed.ncbi.nlm.nih.gov/33384352/)
 79. C. Y. Liu, Z. Xu, R. J. Kaufman, Structure and intermolecular interactions of the luminal dimerization domain of human IRE1alpha. *J. Biol. Chem.* **278**, 17680–17687 (2003). doi: [10.1074/jbc.M300418200](https://doi.org/10.1074/jbc.M300418200); pmid: [12637535](https://pubmed.ncbi.nlm.nih.gov/12637535/)
 80. L. Buscail, B. Bournet, P. Cordelier, Role of oncogenic KRAS in the diagnosis, prognosis and treatment of pancreatic cancer. *Nat. Rev. Gastroenterol. Hepatol.* **17**, 153–168 (2020). doi: [10.1038/s41578-019-0245-4](https://doi.org/10.1038/s41578-019-0245-4); pmid: [32005945](https://pubmed.ncbi.nlm.nih.gov/32005945/)

81. A. W. Tolcher *et al.*, Antitumor activity in RAS-driven tumors by blocking AKT and MEK. *Clin. Cancer Res.* **21**, 739–748 (2015). doi: [10.1158/1078-0432.CCR-14-1901](https://doi.org/10.1158/1078-0432.CCR-14-1901); pmid: [25516890](#)
82. V. Chung *et al.*, Effect of selumetinib and MK-2206 vs oxaliplatin and fluorouracil in patients with metastatic pancreatic cancer after prior therapy: SWOG S1115 study randomized clinical trial. *JAMA Oncol.* **3**, 516–522 (2017). doi: [10.1001/jamaonc.2016.5383](https://doi.org/10.1001/jamaonc.2016.5383); pmid: [27978579](#)
83. N. Zhao *et al.*, Pharmacological targeting of MYC-regulated IRE1/XBP1 pathway suppresses MYC-driven breast cancer. *J. Clin. Invest.* **128**, 1283–1299 (2018). doi: [10.1172/JCI95873](https://doi.org/10.1172/JCI95873); pmid: [29480818](#)
84. P. J. Le Reste *et al.*, Local intracerebral inhibition of IRE1 by MKC8866 sensitizes glioblastoma to irradiation/chemotherapy in vivo. *Cancer Lett.* **494**, 73–83 (2020). doi: [10.1016/j.canlet.2020.08.028](https://doi.org/10.1016/j.canlet.2020.08.028); pmid: [32882336](#)
85. S. E. Logue *et al.*, Inhibition of IRE1 RNase activity modulates the tumor cell secretome and enhances response to chemotherapy. *Nat. Commun.* **9**, 3267 (2018). doi: [10.1038/s41467-018-05763-8](https://doi.org/10.1038/s41467-018-05763-8); pmid: [30111846](#)
86. N. Y. Gabrai *et al.*, A phase 1/2 trial of ORIN1001, a first-in-class IRE1 inhibitor, in patients with advanced solid tumors. *J. Clin. Oncol.* **39** (15_suppl), 3080–3080 (2021). doi: [10.1200/JCO.2021.39.15_suppl.3080](https://doi.org/10.1200/JCO.2021.39.15_suppl.3080)
87. M. Salmon *et al.*, Kras oncogene ablation prevents resistance in advanced lung adenocarcinomas. *J. Clin. Invest.* **133**, e164413 (2023). doi: [10.1172/JCI164413](https://doi.org/10.1172/JCI164413); pmid: [36928090](#)
88. H. C. Mahler, W. Friess, U. Grauschof, S. Kiese, Protein aggregation: Pathways, induction factors and analysis. *J. Pharm. Sci.* **98**, 2909–2934 (2009). doi: [10.1002/jps.21566](https://doi.org/10.1002/jps.21566); pmid: [18823031](#)
89. M. F. Rimawi *et al.*, Early efficacy evaluation of ORIN1001, a first in class IRE1 alpha inhibitor, in advanced solid tumors. *J. Clin. Oncol.* **41** (16_suppl), 1092–1092 (2023). doi: [10.1200/JCO.2023.41.16_suppl.1092](https://doi.org/10.1200/JCO.2023.41.16_suppl.1092)
90. M. P. Kim *et al.*, Generation of orthotopic and heterotopic human pancreatic cancer xenografts in immunodeficient mice. *Nat. Protoc.* **4**, 1670–1680 (2009). doi: [10.1038/nprot.2009.171](https://doi.org/10.1038/nprot.2009.171); pmid: [19876027](#)
91. L. Yan *et al.*, Targeting glucose metabolism sensitizes pancreatic cancer to MEK inhibition. *Cancer Res.* **81**, 4054–4065 (2021). doi: [10.1158/0008-5472.CAN-20-3792](https://doi.org/10.1158/0008-5472.CAN-20-3792); pmid: [34117030](#)
92. Z. Cheng *et al.*, Inhibition of BET bromodomain targets genetically diverse glioblastoma. *Clin. Cancer Res.* **19**, 1748–1759 (2013). doi: [10.1158/1078-0432.CCR-12-3066](https://doi.org/10.1158/1078-0432.CCR-12-3066); pmid: [23403638](#)
93. N. E. Sanjana, O. Shalem, F. Zhang, Improved vectors and genome-wide libraries for CRISPR screening. *Nat. Methods* **11**, 783–784 (2014). doi: [10.1038/nmeth.3047](https://doi.org/10.1038/nmeth.3047); pmid: [25075903](#)
94. P. Bankhead *et al.*, QuPath: Open source software for digital pathology image analysis. *Sci. Rep.* **7**, 16878 (2017). doi: [10.1038/s41598-017-17204-5](https://doi.org/10.1038/s41598-017-17204-5); pmid: [29203879](#)
95. K. H. Wrighton *et al.*, Small C-terminal domain phosphatases dephosphorylate the regulatory linker regions of Smad2 and Smad3 to enhance transforming growth factor- β signaling. *J. Biol. Chem.* **281**, 38365–38375 (2006). doi: [10.1074/jbc.M607246200](https://doi.org/10.1074/jbc.M607246200); pmid: [17035229](#)
96. B. C. Cross *et al.*, The molecular basis for selective inhibition of unconventional mRNA splicing by an IRE1-binding small molecule. *Proc. Natl. Acad. Sci. U.S.A.* **109**, E869–E878 (2012). doi: [10.1073/pnas.1115623109](https://doi.org/10.1073/pnas.1115623109); pmid: [22315414](#)
97. S. V. Vasaikar, P. Straub, J. Wang, B. Zhang, LinkedOmics: Analyzing multi-omics data within and across 32 cancer types. *Nucleic Acids Res.* **46** (D1), D956–D963 (2018). doi: [10.1093/nar/gkx1090](https://doi.org/10.1093/nar/gkx1090); pmid: [29136207](#)

ACKNOWLEDGMENTS

We thank J. Rosen, Q. Zhang, and J. Xu for advice, discussion, and critical review of the manuscript. **Funding:** This work was supported by US Department of Defense Congressionally Directed Medical Research Programs (W81XWH1910524 to X.C., W81XWH1910035 to X. Lv), the National Institutes of Health (R01CA270240, R37CA228304, P50CA186784, and R01HL146642 to X.C.; R01CA214793 and 5P01CA117969 to H.Y.; R01CA272744 to W.Y.; R01DK115454 and R01GM142143 to A.C.; T32DK60445-17 to L.M.; CA21591 and SPORE DRP CA126752 to Z.S.; U24CA210954 to B.Z.; U54CA224065 and U54CA224081 to J.A.R.; R01GM130838 and R01NS117668 to Y.C., and R01HD007857 and R01HD008188 to B.W.O.), Cancer Prevention and Research Institute of Texas (RP230285 to X.C., RRI40038 CPRIT Scholar in Cancer Research award to A.C., RP160283 Baylor College of Medicine Comprehensive Cancer Training Program award to F.P., and RR160027 CPRIT Scholar in Cancer Research award to B.Z.), and American Cancer Society (RSG-22-017-01-CCB to W.Y.). This work used the Aperio GT-450 digital pathology scanner in the Baylor College of Medicine Breast Center Pathology Core that was purchased with funding from the NIH S10 grant S10OD028671. This work was supported by the Cytometry and Cell Sorting Core at the Baylor College of Medicine with funding from the CPRIT Core Facility Support Award (CPRIT RP180672), the NIH (CA125123, S10OD025251, and RR024574), and the assistance of J. M. Sederstrom. Imaging for this work was supported by the Integrated Microscopy Core at the Baylor College of Medicine with funding from NIH (DK56338 and CA125123) and CPRIT (RP150578). This work was supported by the DNA Sequencing Core at the Baylor College of Medicine with funding from the NIH support (R01HD100535) and the assistance of Y. Lei and P. Pimienta Ramirez. **Author contributions:** X.C., H.Y., X. Lv, and X. Lu conceived the project and designed the research. X. Lv, X. Lu, J.C., Y.D., Q.L., Fa.P., D.L., D.H., E.M., D.W.C., X.W., S.M., J.Y., Fe.P., L.Y., L.M., and Y.H. performed the experiments and analyzed the data. H.M., A.P., Y.C., W.Y., E.C.C., A.C., X.Li., G.M., B.B., J.W., P.H., Z.S., H.W., J.A.R., B.W.O., Q.C.Y., M.J.E., and M.F.R. contributed to discussions, experimental design, and critical reagents. S.R.S. and B.Z. analyzed the CPTAC data. X.C. supervised the project. X.C., X. Lv, and X. Lu wrote the paper. **Competing interests:** M.F.R. received research funding from Pfizer and Genentech. M.F.R. is a consultant and receives consulting fees from Novartis, Seagen, Macrogenics, and AstraZeneca. M.F.R. is the principal investigator of the clinical trial NCT03950570. X.C. reports previous research funding from Fosun Pharma. J.A.R. reports receiving a commercial research grant from The University of Texas MD Anderson Cancer Center, has a sponsored research agreement from Genprex, has ownership interest (including stock, patents, etc.) in Genprex, and is a consultant and advisory board member for Genprex. M.J.E. reports full-time employment with AstraZeneca from 7 March 2022. M.J.E. holds patents and receives income from Veracyte on the PAM50-based products, Prosigna. **Data and materials availability:** All data are available in the manuscript or the supplementary materials. Requests for materials should be addressed to X.C. **License information:** Copyright © 2023 the authors; some rights reserved; exclusive licensee American Association for the Advancement of Science. No claim to original US government works. <https://www.science.org/about/science-licenses-journal-article-reuse>

SUPPLEMENTARY MATERIALS
science.org/doi/10.1126/science.abn4180
 Figs. S1 to S18
 Tables S1 to S5
 MDAR Reproducibility Checklist

Submitted 24 November 2021; resubmitted 6 March 2023
 Accepted 28 July 2023
 10.1126/science.abn4180